Received: 14 October 2020 | Revised: 27 November 2020 | Accepted: 8 January 2021

DOI: 10.1002/arp.1809

RESEARCH ARTICLE

WILEY

# The Yığma Tepe of Pergamon: Internal construction of a monumental burial mound from shear wave reflection sounding and wavefield modelling

Rebekka Mecking[1,2] | Matthias Meinecke[3] | Ercan Erkul[1] | Felix Pirson[4] | Wolfgang Rabbel[1]

[1]Institute for Geosciences, Kiel University, Kiel, 24118, Germany

[2]S1 - Seismic, Gravimetry, and Magnetics, Leibniz Institute for Applied Geophysics, Hannover, 30655, Germany

[3]Faculty of History, Arts and Oriental Studies, Classical Archaeology, Leipzig University, Leipzig, 04109, Germany

[4]Department Istanbul, German Archaeological Institute (DAI), Istanbul, 34437, Turkey

**Correspondence**
Rebekka Mecking, Institute for Geosciences, Kiel University, Otto-Hahn-Platz 1, Kiel 24118, Germany.
Email: rebekka.mecking@ifg.uni-kiel.de

**Funding information**
Agence nationale de la recherche (ANR); Deutsche Forschungsgemeinschaft (DFG), Grant/Award Number: 246601872; German Archaeological Institut (DAI)

## Abstract

The Yığma Tepe of Pergamon is one of the largest known burial mounds in the Eastern Mediterranean. Its internal structure, especially the existence and location of burials, remains unknown so far because its height of 32 m and the diameter of 158 m have restricted extensive excavations. To explore the interior of the Yığma Tepe, we applied shear wave reflection profiling and traveltime tomography, locally complemented by electrical resistivity tomography. Shear wave reflection imaging enabled us to identify the layering and localize structures down to the basal surface of the mound with a metre-scale resolution. A grid of crossing SH-wave profiles with 4-m line spacing covered the central mound area. The Yığma Tepe can be subdivided into three stratigraphic layers representing different construction phases, each about 10 m thick. The deepest is a consolidated layer with a locally compacted surface. SH-wave reflection imaging verified the collapsed remains of a tunnel system and a shaft at about 30-m depth that had been dug into the mound at the level of the basal surface at the beginning of the 20th century. The tunnel collapse created a damage zone of decreased S-wave velocity reaching up to the overlying middle layer, in which four seismic objects of interest (SOIs) were detected. The largest of these SOIs is a north–south-oriented structure, about 15 m long and 4 m wide. SH-viscoelastic forward modelling showed that it likely consists of a collapsed walled cavity with a zone of loosened soil above. The third layer covers the underlying two and is enriched with large stone packages as verified by local excavations. We show the capabilities of shear-wave reflection seismic to image small-scale structures under complicated topographic conditions and how characteristics of cavities and volumes of decompacted soil can be evaluated by wavefield modelling.

## 1 | INTRODUCTION

The Yığma Tepe is a monumental mound near the ancient city of Pergamon in Turkey (Figure 1a) and is part of the UNESCO World Heritage. It has a height of ~32 m and a diameter of ~158 m, comparable with the well-known Kastas tumulus in Northern Greece or the tumulus on the Nemrut Dağı in the southeast of Turkey. Due to this enormous size, it is assumed that it contains the burial place of an

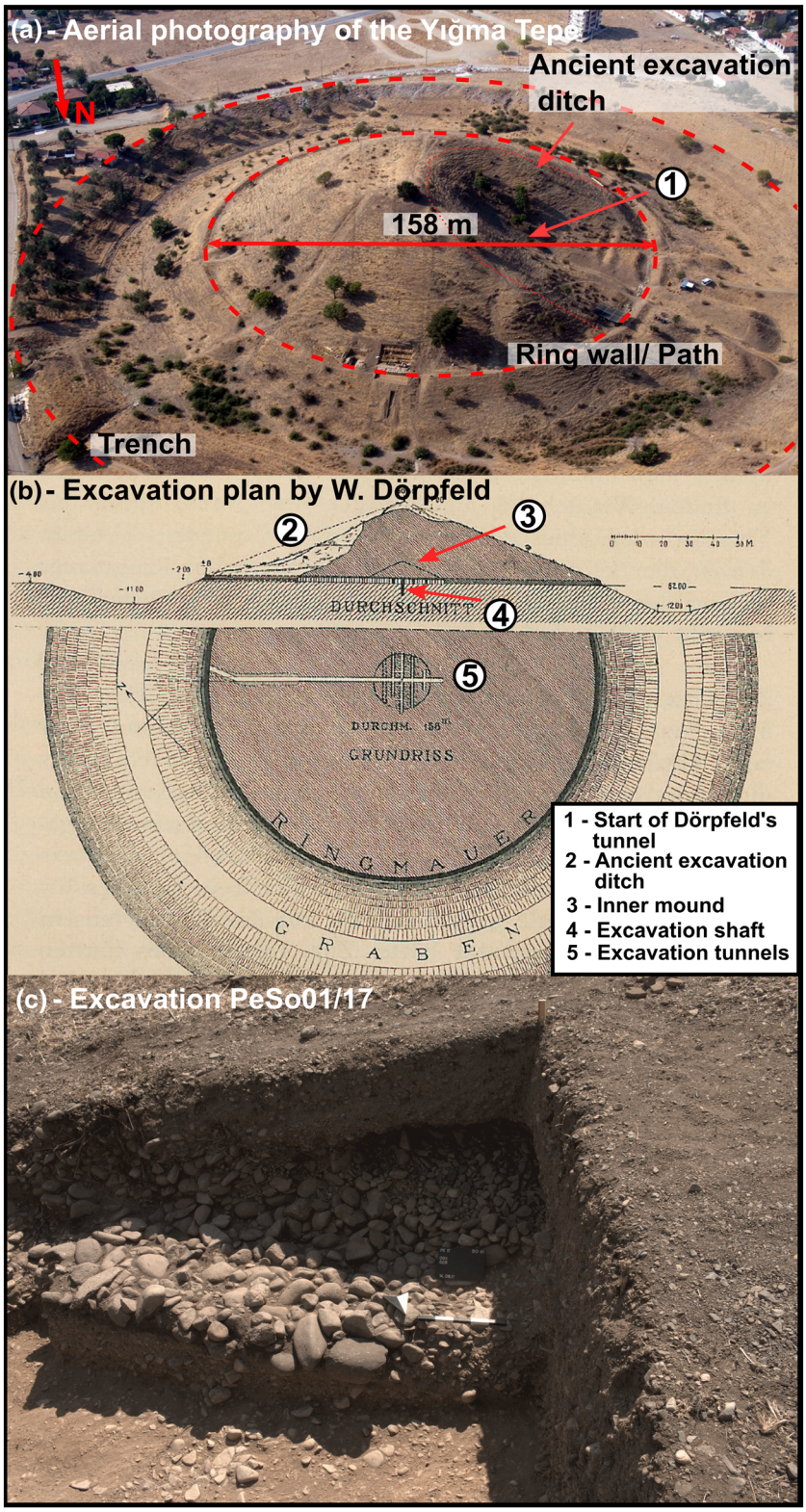


**FIGURE 1** (a) Aerial photography of the Yığma Tepe by B. Ludwig (DAI Istanbul, September 2015); (b) Dörpfeld's map of the Yığma Tepe, drawn during his excavations (Dörpfeld, 1910). His excavated tunnel system is visible in the ground view (bottom). 'Ringmauer' indicates the surrounding wall (crepis). 'Graben' indicates the trench which surrounds the tumulus. (c) Rubble accumulation found in sondage PE17/So01 (photograped by M. Meinecke, September 2017)

important resident or ruler of the ancient city of Pergamon. It has been cautiously dated to the second century BC (Kelp, 2014; Pirson, 2017).

From 1905 to 1909, the Yığma Tepe was intensively investigated by the German archaeologist Wilhelm Dörpfeld and his team (Dörpfeld, 1910). They excavated the massive ring wall surrounding the mound and drove a tunnel to the centre of the mound in search of a grave chamber. However, the efforts were not successful. Despite additional transversal tunnels and extensive search drillings, driven from the centre of the mound in all directions, no evidence of burials was found. Also, the search for the entrance of an access tunnel (dromos) along the ring wall was not successful.

The work of Dörpfeld basically defined the state of knowledge about the Yığma Tepe until 2014. Since then, until 2019, the mound has been reinvestigated by our team within a collaborative French–German–Turkish project on the funerary landscape and customs in Pergamon and other ancient cities of the Aiolis (Kelp, 2014; Pirson, 2016). To gain a most comprehensive understanding of the construction of Yığma Tepe, we applied a combined approach of geophysical prospecting and archaeological test excavations.

In the past, monumental burial mounds were investigated rarely because both geophysical sounding and excavations require unusually high technical efforts. In the eastern Mediterranean, experience in geophysical prospection was gained, for example, at Kastas tumulus in Amphipolis (Greece) where P-wave seismic tomography (Polymenakos & Tweeton, 2017) and 3D electrical resistivity tomography (ERT) (Tsokas et al., 2018) were performed to clarify the geological structure and identify targets of interest for future excavations. Lütjen and Utecht (1991) used P-wave seismic measurements and Ground Penetrating Radar (GPR) to image the interior of the Nemrut Dağı in southeastern Turkey to locate burial chambers. They got some information on the stratification of the mound but did not identify any grave structures. Forte and Pipan (2008) used P-wave seismic tomography in combination with GPR measurements to image the interior of a small burial mound in northern Italy where seismic tomography extended the limited depth imaging capabilities of the GPR reflection image, allowing to precisely locate the grave. Also, magnetic surveys (Parzinger et al., 2016) were successfully used to identify burial structures at and around small burial mounds in Kazakhstan whereas microgravity measurements were used to detect an undgeround mausoleum in a grave mound in China (Shiyi et al., 2006).

In the present paper, we focus on investigating the internal structure of the Yığma Tepe through shear wave (S-wave) reflection profiling. The reason for applying S-waves is their capability to fulfil the survey requirements consisting of resolving targets with diameters smaller than 5 m and depths of up to 30–40 m (a discussion on resolution of S-wave reflection is presented in Section 3). This is remarkable because the geophysical methods usually applied in onshore archaeological prospecting fail in this case: surface-based magnetic and geoelectric measurements do not achieve the required resolution, and ground penetrating radar is usually limited in penetration depth (e.g., Forte & Pipan, 2008).

The objectives of the present study, also defining its outline, are the following:

1. to image the internal structure of the Yığma Tepe by S-wave reflection profiling;
2. to quantify the shape, size and material of possible internal constructions by numerical wavefield modelling;
3. to identify seismic objects of interest (SOIs) based on imaging and modelling results;
4. to evaluate the significance of SOIs in the context of the general seismic stratigraphy of the Yığma Tepe;
5. to draw methodological conclusions on the application of S-wave sounding to complicated near-surface environments.

When interpreting our S-wave reflection data, we take advantage of stratigraphic results previously obtained by refraction profiling with compressional waves (P-waves), ERT and archaeological excavations. They have been published in precursory papers (Mecking et al., 2015, 2016, 2018; Mecking,Köhn, Meinecke, & Rabbel, 2020) and are summarized in Section 2. In seismic data processing and interpretation (Section 3), we rely on common midpoint (CMP) processing in combination with first arrival traveltime tomography and finite difference (FD) wavefield modelling. Accordingly, Section 4 comprises two parts: the first part (Section 4.1) explains the major seismic structures detected by seismic reflection imaging and velocity tomography by exemplary profiles; the second part (Section 4.2) evaluates different hypothetic interpretations inferred by numerical wave-field modelling. The archaeological relevance of the seismic findings is discussed in Section 5.

## 2 | ARCHAEOLOGICAL AND GEOLOGICAL SETTING AND PREVIOUS GEOPHYSICAL INVESTIGATIONS

The Yığma Tepe, with its diameter of ∼158 m and a height of ∼32 m, is the largest burial mound around the ancient city of Pergamon and one of the largest in the eastern Mediterranean. It is surrounded by an ∼62 m wide and ∼12 m deep trench. The soil, which originally filled the trench, was used to construct the mound. At its base, at ∼41.5 m above sea level (ASL), the mound is surrounded by an originally 3 m wide and 2 m high ring wall of large tuff blocks, called crepis, which is only partially preserved.

The mound and surrounding soil consist of river sediments from the rivers Bakır Çayı (ancient: Kaïkos) and Bergama Çayı (ancient: Selinus) (Philippson, 1912). They consist of layers of sand and gravel with maximum diameters of 0.5 m (Mecking et al., 2020). Refraction seismic measurements showed that two overlapping alluvial fans exist in the area of the Yığma Tepe, distinguishable by their P-wave velocity and composition.

The mound consists of three construction phases, each about 10 m high, which could be distinguished by their P-seismic velocities (Mecking et al., 2020; Mecking et al., 2015, 2016, 2018). Phase 1 located at the basal surface of the mound shows significantly higher seismic velocities (ca. 800 m/s) than the two phases above it (∼500 and 400 m/s, respectively) (Figure 2a). As the same applies to the shear wave velocities, to be shown in Section 4.1.1 and as there are no indications the density shows a significantly different behaviour, this implies also an increase in shear and compressional strength (e.g., Schön, 2015) indicating increased compaction and stability at depth. The measurements did not distinguish whether only the surface layer of this first construction phase is compacted or if Phase 1 is homogeneously consolidated. A thin layer with the same P-wave velocity as Phase 1 (800 m/s) was found at the top of the mound and excavated for verification in 2017 (Mecking et al., 2020; Meinecke, 2019a). The excavations showed that the high-velocity layer has a higher content of clay, silt and fine sand than the surrounding soil and an increased stiffness making it suitable for a foundation for buildings.

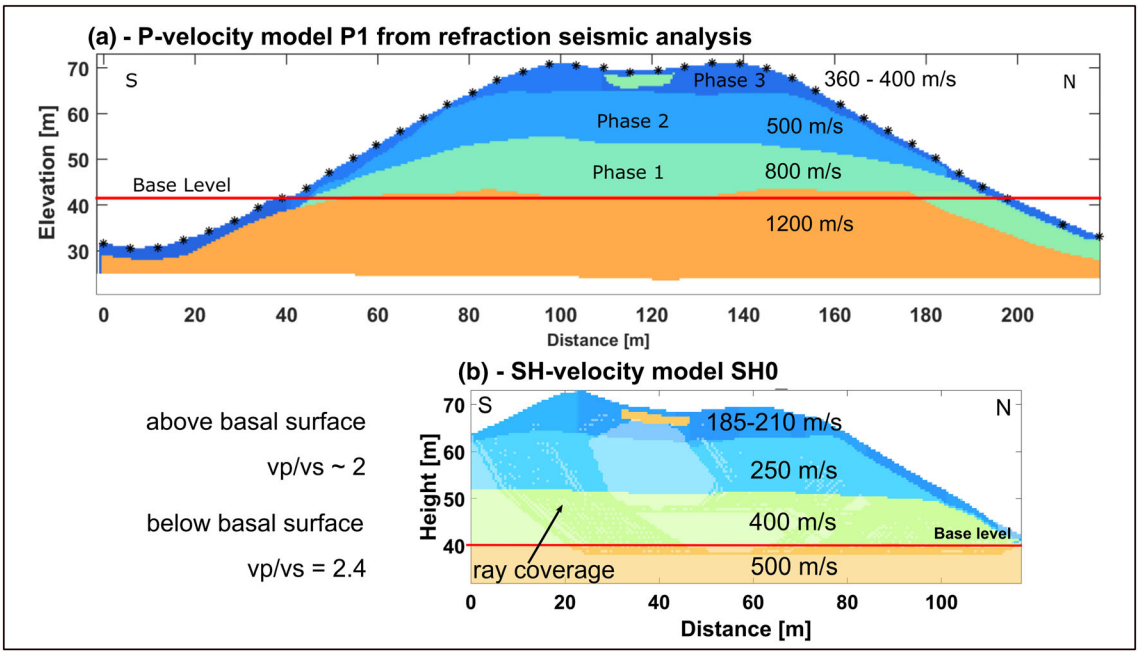


**FIGURE 2** (a) Result of the P-refraction seismic velocity analysis (Mecking et al., 2020) showing the three construction phases of the tumulus above a relatively flat basal surface. (b) The layer elevations are used in the building process of the SH-velocity model. Interactive fitting of the traveltime branches is performed, finetuning of velocities and layer topography

The surface of the Yığma Tepe shows a number of remains of illicit excavation attempts, the largest of which is a mighty ditch extending radially from the top in the northwest direction (Figure 1a). Despite this, it is generally assumed that internal grave constructions, if they exist at all, are still undisturbed (Radt, 2016). The first archaeological excavation took place under the supervision of Wilhelm Dörpfeld from 1905 to 1909, whose team excavated the ring wall surrounding the mound hoping to find an access corridor (or dromos) to a burial site, and the team also drove a tunnel from the ancient ditch in the northwest to the centre of the mound, from where it perforated the central volume with a system of smaller transversal tunnels and drillings searching for a burial chamber (Figure 1b). At the geometric centre of the circular ring wall, he found the remains of two wooden posts, probably having served for defining the centre of the mound at the very beginning of its construction. Unfortunately, these posts are lost, so no dating is possible. At the position of these posts, a well was dug to 2 m below the basal surface, but without any findings of archaeological relevance (Dörpfeld, 1910). Within 3 years, part of the tunnel framework became rotten due to the humidity inside the mound. In 1909, at the end of the disappointing campaign, Dörpfeld had the remaining preserved parts of the tunnel framework removed and the entrance to the tunnel system destroyed. His work has shown that a burial chamber is not located in the centre of the burial mound, if there is one at all. From today's perspective, it demonstrates the need for extensive prospection using nondestructive methods prior to major excavations.

From 2015 to 2019, small test excavations were carried out at the surrounding ring wall and at the top of the mound to gain information on the mound's construction and to find datable material. Among other things, rubble walls were found behind the ring wall, running radially towards the centre of the mound with regular spacing of approximately 1 m, a thickness of about 0.2 m and a height of up to 0.74 m, apparently serving to stabilize the mound (Meinecke, 2019b; Pirson, 2016). They consist of larger stones originating from the sediment layer in the area. Similar radial but also concentric walls were discovered in the excavations at the mound's top, seeming to be partially oriented towards the centre of the mound (Meinecke, 2019a). Directly in the centre of the mound at 1.5 m below the top's surface (Figure 3, Pe17/So04), a strongly hardened layer was found, matching a high-velocity zone (HVZ) detected before by P-wave refraction measurements (Mecking et al., 2020).

In the excavations behind the ring wall at levels higher than the wall, in the ancient robbery trench and on the northern top zone, alternating layers of gravelly sand and large rubble were found in the profile, seeming to be part of the original embankment. Later, these layers were modified close to the surface due to the use of the mound as a vineyard in the 19th and beginning of 20th century (Meinecke, 2019a).

## 3 | DATA ACQUISITION AND INTERPRETATION METHODS

### 3.1 | Benefits and limitations of SH-wave profiling

To explore a burial mound the size of the Yığma Tepe for building structures down to the level of the basal surface, seismic methods are the first choice, because they are the only ones capable of resolving

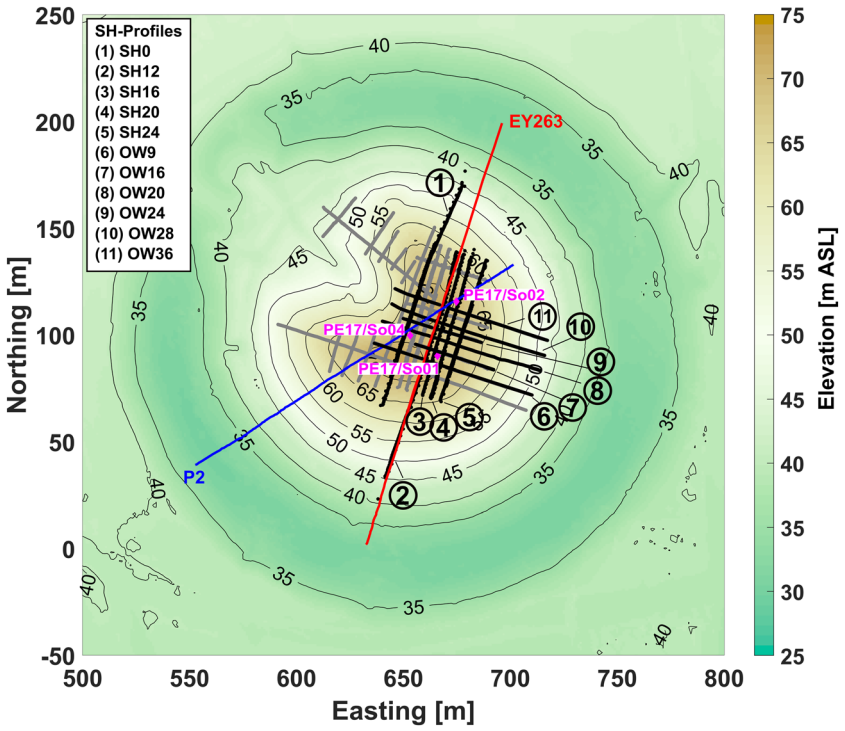


**FIGURE 3** Topographical map of the Yığma Tepe. Measured SH-seismic profiles are depicted in grey, profiles in this paper in black. The location of the P-seismic profile (Figure 2) is shown in blue; the geoelectric profile (Figure 10) is shown in red. Excavations at the top of the tumulus are marked in pink

the subsoil with a resolution of a few metres at depths of several tens of metres. Whereas refraction seismic measurements with P-waves were used to create a seismic stratigraphic model, we chose SH-wave reflection seismic for searching metre-scale bodies such as burial chambers.

SH-waves have been used to explore archaeological and geoarchaeological targets sporadically since the 1980s to locate and map silted rivers (Stümpel et al., 1988) and ancient harbours, for instance at Miletus in Turkey (Wölz & Rabbel, 2005) and at Itanos in Greece (Vafidis et al., 2003). Köhn et al. (2019) used full-waveform inversion (FWI) with a near-surface SH-wave data set to map the remains of a medieval channel construction in Southern Germany.

Apart from archaeological investigations, SH-waves are used to investigate near-surface stratigraphy because they exhibit a higher spatial resolution than P-waves and are not influenced by the water content of the soil (Stümpel et al., 1984). In recent years, there were some applications in the location of sinkholes and subrosion structures (Krawczyk et al., 2012) as well as in lignite exploration (Milkereit et al., 1986), which used conventional CMP processing.

In soils, shear wave velocity is typically by a factor 0.1–0.5 slower than P-wave velocity (Schön, 2015; Stümpel et al., 1984). Because the wavelength is proportional to the wave velocity for a given signal frequency, the spatial resolution of S-wave reflection imaging is improved by a factor of 2–10 compared with P-wave imaging if the same signal frequencies are considered (Stümpel et al., 1984). In the present case, the average velocities inside the burial mound range from 180 to 260 m/s, although the main frequency is about 50 Hz, decreasing to about 30 Hz for the later reflections. Vertical resolution determined by the quarter-wavelength ($\lambda/4$) criterion thus ranges from less than 1–2.3 m. The horizontal resolution of unmigrated seismic reflection images is usually described by the radius of the first Fresnel zone given by $(z\lambda/2 + \lambda^2/16)^{1/2}$, where $z$ is depth, but it can be improved by migration, which brings it to the same order as the vertical resolution (e.g., Yilmaz, 2001). SH-wave resolution for the present study is discussed in detail in Section 3.3.

Another benefit of S-wave profiling is the so-called reflection window of shallow targets (e.g., Rabbel, 2008). In a P-wave survey, the near-offset range is often heavily disturbed by interfering Rayleigh waves travelling at about S-wave velocity. This often restricts the range of usable P-wave reflections to larger offsets only (e.g., Hunter et al., 1984). In surveys using horizontally polarized S-waves (SH-waves), the corresponding surface waves, namely, Love waves, travel with about the velocity of the direct S-wave. Therefore, they leave the near-offset range unaffected and interfere with shallow reflections at far offsets only (e.g., Wölz & Rabbel, 2005). This is essential for the resolution of near-surface structures whose reflections are hardly detectable at larger offsets as they interfere with direct, refracted and surface wave arrivals.

Despite all these benefits, shear wave applications may face some technical problems. One of them is the coupling of the source to the subsurface; thus, special care has to be taken to prevent horizontal slip depending on the soil conditions. The force transmittable to the ground is usually confined by friction, limiting the penetration depth. More efforts with the receivers are required than with the usual P-wave surveys, because horizontal geophones or, even better, three-component geophones, need to be carefully oriented and anchored in the soil. Due to their short wavelength, S-waves are more sensitive to small-scale heterogeneity and are more exposed to absorption than P-waves. Both effects cause increased efforts in data processing.

### 3.2 | Seismic data acquisition

Between 2014 and 2018, a total of 25 SH-wave profiles were collected on the Yığma Tepe (Figure 3). Inline and crossline profiles covered the central mound area on a rectangular grid with profile spacings of 4 m. Because the structures of interest typically have dimensions of a few metres in diameter, dense cross-profile measurements are necessary to identify them and to determine their extensions. The investigation was focused on the central burial mound. The flanks of the mound were also examined in part by extended and additional profiles.

The lengths of the profiles ranged from 12 to 120 m with a geophone spacing of 0.5 m. The signals were recorded by up to 10 24-channel GEODE registration units, so up to 240 channels in total per profile. Acquisition parameters are listed in more detail in Table A2.

We generated the S-wave signals by horizontal hammer blows on a vertical iron plate. This was either fit to the sidewalls of small pits or attached to a steel bar pressed to the ground depending on the soil and terrain conditions (Figure 4). Hammer blows and receivers were both oriented perpendicular to the profile direction.

### 3.3 | Shear wave velocity determination

To determine the S-wave velocity structure of the Yığma Tepe, we inverted the first arrival traveltime branches using the interactive raytracing module of the ReflexW software package (Sandmeier, 2019). The forward calculation of the traveltimes is based on an FD approximation of the eikonal equation (Vidale, 1988). The raypath is computed on a uniform grid with a grid spacing of 0.5 m.

Waves refracted through the deeper parts of the mound could only be observed on profiles with spread lengths longer than 100 m. For the velocity analysis, Profile SH0 with a length of 120 m was used. Particularly in the central area of the mound's top, the picking of first SH-wave arrivals was complicated by the occurrence of converted P-waves generated by the 3D heterogeneity of the near-surface soils (Figure 5a). This heterogeneity is caused by stone settings and local compaction as verified by excavations (Mecking et al., 2020; Mecking et al., 2016, 2018). This hetereogeneity produces HVZs, additionally reducing the ray coverage of the mound (Figure 2b).

We used the seismic stratigraphic information known from a previous P-refraction seismic analysis based on interactive layer and velocity fitting (Figure 2a; Mecking et al., 2020), when placing the initial layer boundaries, adapted the velocity to fit the traveltimes and then further adapted the layer boundaries to improve the traveltime fit. A mean root mean square (RMS) error of 8 ms was achieved on 78 picked shots. Picking inaccuracy was ~1 ms outside the top area of the mound.

Comparing the P-wave and SH-wave velocity models (Figure 2) yields a $V_P/V_S$-ratio of 2 for all three layers above the basal surface of the mound. The ratio increases to 2.4 for the undisturbed soil below the mound, values common for unconsolidated soils (e.g., Schön, 2015).

For the other SH-profiles, a velocity analysis of the deeper parts of the mound was not possible due to the missing ray coverage. Therefore, we adapted the values from profile SH0 (cf. Figure A2).

### 3.4 | Seismic reflection processing

The seismic data of the different profiles show a uniformly high signal-to-noise ratio, impaired only little by the noise of the surrounding city. Example shots are shown in Figure 5. The frequency-time spectrum shows that the signal energy concentrates between 30 and 80 Hz between 50 and 150 ms of traveltime. For larger traveltimes, the centre frequency decays to 30 Hz (Figure 5b). Above 100 Hz, ambient noise dominates the records; therefore, a bandpass with 80-Hz high cut was applied for display (cf. Table A1).

From 0.05 to 0.25 s of traveltime, the records show many short segments of partly interfering reflected arrivals, partly hyperbolae

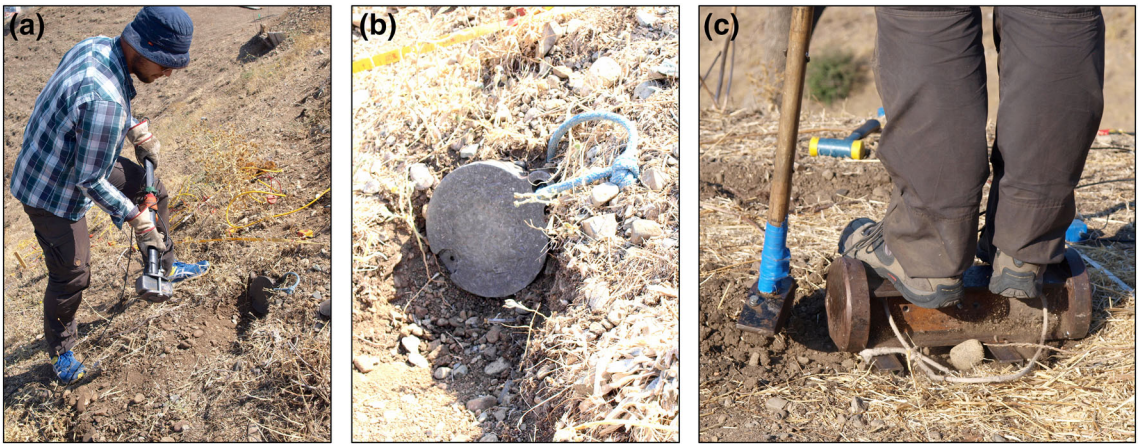


**FIGURE 4** SH-sources: (a) Hammer blow on a vertically standing (a, b) iron plate or an (c) iron bar (photography by W. Rabbel, September 2015 [b, c] and September 2017 [a])

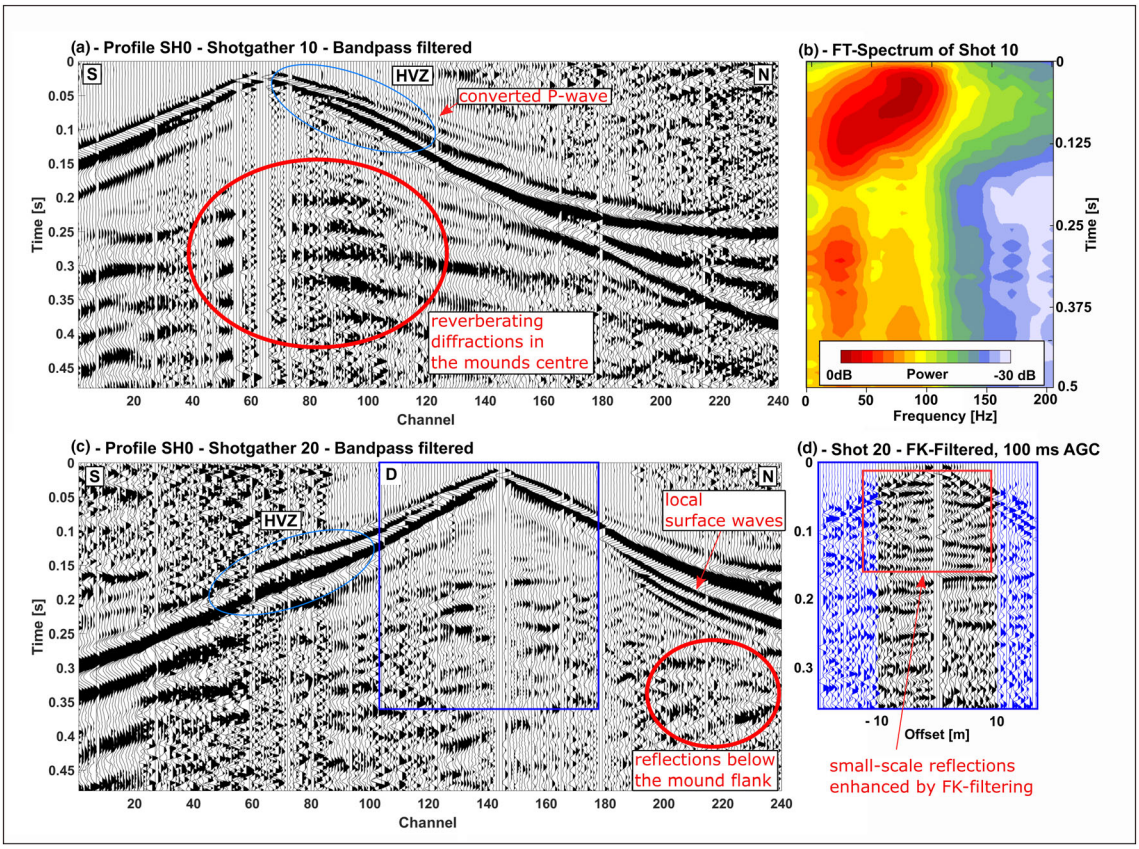


**FIGURE 5** (a, c) Two bandpass-filtered example shot gathers on SH-profile SH0 (*F* = 10, 20, 80 and 100 Hz). (b) Time-variant frequency spectrum for shot 10. (d) Example of FK-filtering. Traces <10-m offset are included in the CMP stack (d, black wiggles). The central shots are dominated by reverberating diffractions. Converted P-waves increase the picking difficulty. Local surface waves and backscattering from the surface signals need to be handled during processing. Further data and processing examples are given in Appendix A

from buried scattering objects, partly side reflections from surface disturbances (Figure 5a,c,d). In contrast, the seismogram is dominated by a low-frequency band of coherent hyperbolic arrivals between 0.2 and 0.4 s. The apex of these reverberating diffractions is situated exactly at the centre of the mound. Figure 5c also shows a diffraction hyperbola originating at the western (right hand) end of the profile, observable along the mound's flank.

Some wavefield perturbations are caused by the 3D heterogeneity of the very near-surface soils. These occur in the form of P-wave arrivals sporadically emerging from SH-waves due to 3D scattering and in form of local dispersive surface waves and backscattered direct waves. To avoid interference with reflections and diffractions from deeper interfaces, these signals were removed prior to CMP processing by surgical muting, FK filtering and limiting the offset of CMP gathers to a maximum of 10 m. For the CMP processing, we applied the Globe Claritas software (created by GNS Science, Wellington, New Zealand). The processing tests revealed that limiting the source–receiver offsets of the traces used in the CMP stack as well as shot-wise adapted front muting was the major step to improve the quality of the stacked sections at near-surface levels. Near-offset reflections get otherwise overlain in CMP stacking by strong-amplitude remains of direct and surface waves from larger offsets that survived the stretch muting (cf. Figure A3). With the reduced offset range, CMP coverage is still tenfold to 13-fold along most parts of the profiles.

Offset limitation, discontinuous reflections and topographic effects caused standard CMP velocity analysis to be of little significance. Therefore, we derived normal moveout correction (NMO) corrections from the velocity field obtained from the interactive raytracing described above via Dix's formula (Dix, 1955; Section 3.3; Figure A2). The interval S-wave velocities range from 180 m/s at the surface up to 500 m/s at the base, leading to RMS velocities from 180 to 260 m/s.

After some tests, poststack FD migration was chosen to migrate the CMP-stacked sections. Tests comparing FD, Kirchhoff and Stolt time migrations are presented in Figure A4. Kirchhoff migration smoothed out many small-scale reflections, partly creating artifact reflections from the scattered signals, partly erasing the heterogeneous structure. The same applies to prestack/poststack depth conversion. In contrast, both FD migration and Stolt migration performed well in focusing the scattering arrivals visible in the stack.

We paid special attention to imaging diffracting structures equally well at all depth levels from the very near surface down to the basal surface of the mound. For this purpose, we fine-tuned the RMS velocity field by decreasing and increasing it systematically and evaluating the results regarding undermigration and overmigration effects. At the

centre of the mound, optimum focusing occurred at migration RMS velocities of 170–190 m/s, whereas the overall velocity field ranges from 190 to 260 m/s. Therefore, the RMS velocity model was changed accordingly for the final FD migration (Figure A4a,b). In a final step, the time-migrated CMP stack was depth converted using the migration velocity field.

### 3.5 | Viscoelastic forward modelling of SH-waves

Based on seismic reflection imaging, the nature of the reflecting objects can be determined only to a limited extent. Both the shape and the seismic impedance contrasts, generating the backscattered waves remain largely unclear without further investigation. However, for the archaeological interpretation, it is important to distinguish, for example, between an air-filled room, in which no shear waves can propagate, and a massive foundation with increased S-wave velocity and density. Estimates of the size can also help to classify the reflective object.

To clarify the nature of individual reflective elements, we computed synthetic seismograms for a set of hypothetical models derived from the migrated SH-wave reflection sections. Then, the synthetic seismograms were compared with the measured seismograms in order to discriminate the models. For the computations, we used the viscoelastic forward modelling software DENISE (Köhn et al., 2012), a 2D FD code considering SH-wave propagation including Love waves. The application of a 2D code is justified as the objects selected for modelling show a certain linear extension orthogonal to the orientation of the seismic profiles or are symmetric with respect to the profile line. Parameters applied in the forward modelling can be found in Table C1.

In the case of a cavity, not only changing the seismic velocity but also the density has a considerable influence on the backscattering of the seismic waves. Therefore, both velocity and density models were varied in the hypothetic models.

Forward modelling was applied to Profiles SH0 and OW20, intersecting each other at the centre of the mound. The hypothetical models consist of a smooth background velocity distribution based on the calculated interval velocity model, where the scattering structure was embedded.

In designing the hypothetical subsurface models, the following components were considered:

1. The background model for the velocities: For the background velocities, we used smoothed versions of the interval velocity model from the raytracing analysis. For Profile OW20, a mean 1D-model from Profile SH0 was extrapolated (Figure A2). A thin HVZ near the surface had to be inserted to fit the first arrivals.
2. The background model for the density was estimated by assuming a linear relation between S-wave velocity and soil, namely, $\rho$ (kg/m$^3$) = 1,600 + $cV_{SH}$ with proportionality constant $c$ = 1. This relation yields density values in a plausible range for soils (between 1,700 and 2,200 kg/m$^3$; Inazaki, 2006).
3. The intrinsic wave attenuation described by the quality factor $Q$ was determined by test computations assuming different constant $Q$ values. The comparison of computed and observed waveforms at offsets between 0 and 100 m showed optimum similarity at $Q$ = 50.
4. The scattering objects embedded in the background medium were varied in size, shape and position as well as in S-wave velocity and density. Four elements play a key role:
   a. Loosened sediments thought to represent possible cavity fillings represented by S-wave velocities $V_{SH}$ ≤100 m/s and density $\rho \leq$ 1,700 kg/m$^3$.
   b. Cavities represented by shear wave velocities ∼0 m/s and density ∼0 kg/m$^3$.
   c. Compacted soils or walls represented by increased shear wave velocities $V_{SH} \geq$ 600 m/s and increased density $\rho \geq$ 2,200 kg/m$^3$.
   d. Zones of gradual soil loosening ('gradient zones') simulating the stiffness reduction of soils above a collapse, modelled as zones of continuously decreasing shear wave velocity with depth.

### 3.6 | Electric resistivity tomography

To support the interpretation of near-surface seismic structure, we performed ERT (see Figure 3 for location of the profiles). The three overlapping profiles crossing the entire diameter of the mound were measured and inverted as a single profile. The electric data were acquired with a RESECS multielectrode unit (manufactured by GEOSERVE Kiel, Germany) with 1-m electrode spacing in Wenner-Alpha configuration.

Data points showing standard deviations >3% were removed before the inversion. For the ERT, we applied the Res2DInv software (Loke et al., 2013; Loke & Barker, 1995). A robust L1-Norm approach was used for the tomography. It is based on minimizing the sum of absolute values of the residuals of apparent resistivities (L1-norm), which is less sensitive to outliers and scattering data points than a least-squares fit (L2-norm). Local mound topography was incorporated in the inversion. Parameters and other details of the inversion as well as measured and calculated pseudosections and the inverse model prior to topographical correction for Profile E-Y2 are shown in Figure B1. The final model showed an RMS error of 8% (Table B2). The relatively large RMS error is caused by varying electrode coupling in dry heterogeneous soils. The resulting resisitivity model is discussed in Section 4.1.3.

## 4 | RESULTS

### 4.1 | Stratigraphy and localized objects of interest from seismic sounding

The major seismic stratigraphic structure of the Yığma Tepe is known from P-wave refraction seismic investigations (Figure 2a; Mecking et al., 2020). The stratigraphic questions to be approached by S-wave

sounding are the nature of the layer interfaces and the recognition of structures within the layers that could not be resolved by P-waves (Section 4.1.1). It turned out that the S-wave reflection sections show a variety of <5-m to a few 10-m-scale structures in all depth ranges of the mound (consider also the resolution discussion in Figure A1). In the following, we first show the different types of seismic reflection signals using an exemplary profile. Major reflections are then examined for their extent in 3D using cross profiles. Afterwards, the S-wave reflection structure is combined with the stratigraphic model from P/SH-waves (Figure 2) to obtain a comprehensive view of the mound's interior (Section 4.1.2).

### 4.1.1 | General seismic stratigraphy of the Yığma Tepe

We evaluate the SH-wave reflection stratigraphy in comparison with the three major units revealed by refraction profiling using Profile SH0 as an example (Figures 2b and 6a,c showing refraction-derived interfaces in blue and green). Profile SH0 is the only profile for which S-wave refraction interfaces could be determined at all depth levels. Therefore, we use the interface depths of a previously published 3D P-wave velocity model on all other sections for stratigraphic orientation (Figures 6b,d and 7–9).

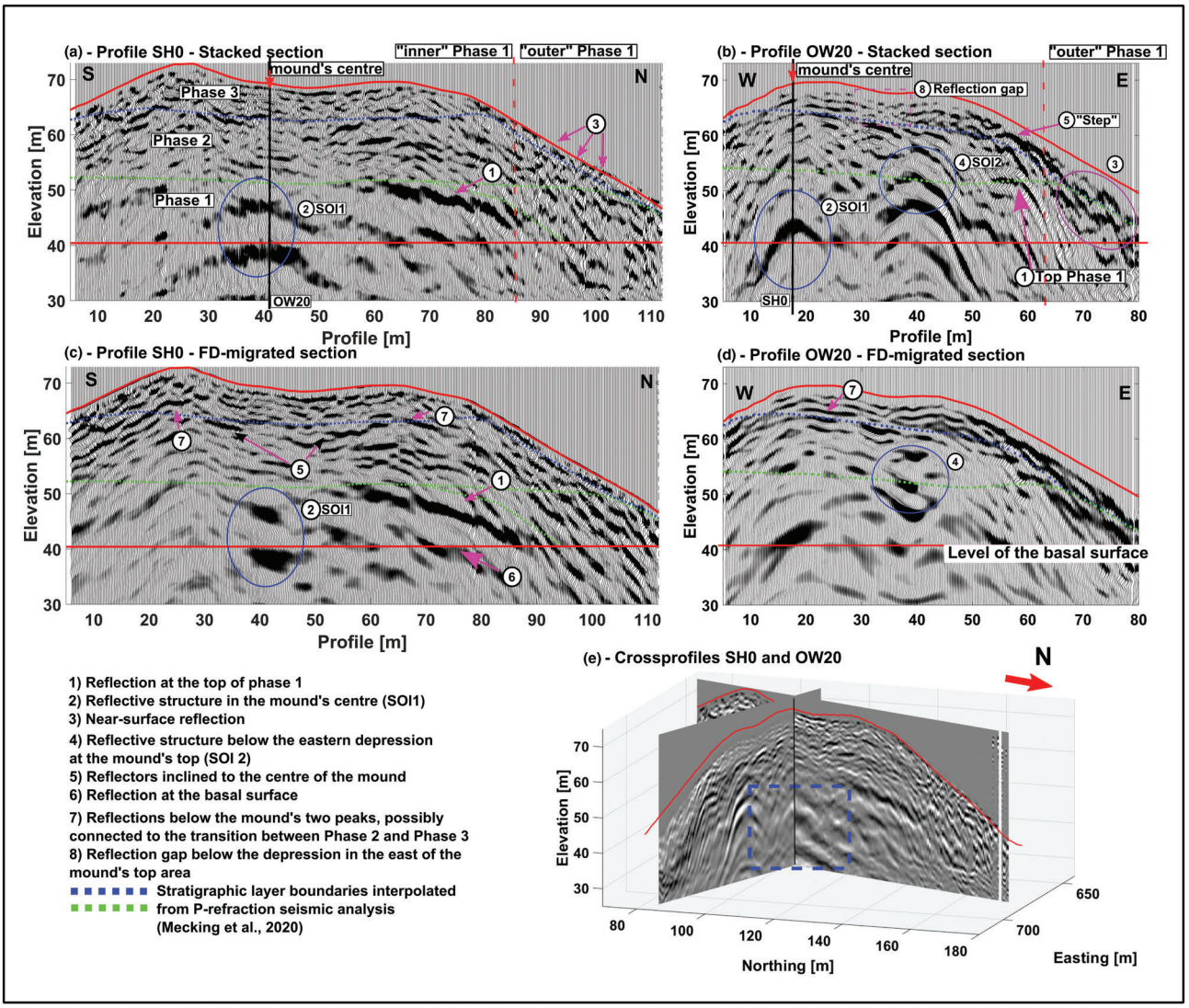


**FIGURE 6** Result of the reflection seismic profiling for (a, c) Profile SH0 and (b, d) Profile OW20. The unmigrated stack of (a) Profile SH0 shows a multitude of reflections above the basal surface (red line). The stack is dominated by reverberating diffractions in the centre of the mound at the level of the basal surface. (c) The finite difference (FD)-migrated stack collapses these diffractions into sharp reflection elements (Marker 2). Similar signals can be observed on (b, d) Profile OW20 (Marker 4) situated higher inside the mound. Distinct, elongated reflections (e.g., Markers 1, 6 and 7) fit the construction phases derived from refraction seismic (green, blue line) and locally also the basal surface derived from the surrounding elevation of the plane (red line). The near surface-area is dominated by chaotic diffracted signals (Marker 3), which are partly eliminated by surgical muting. Also step-like structures can be observed (Marker 5) possibly related to constructions which serve to stabilize the flanks of the mound

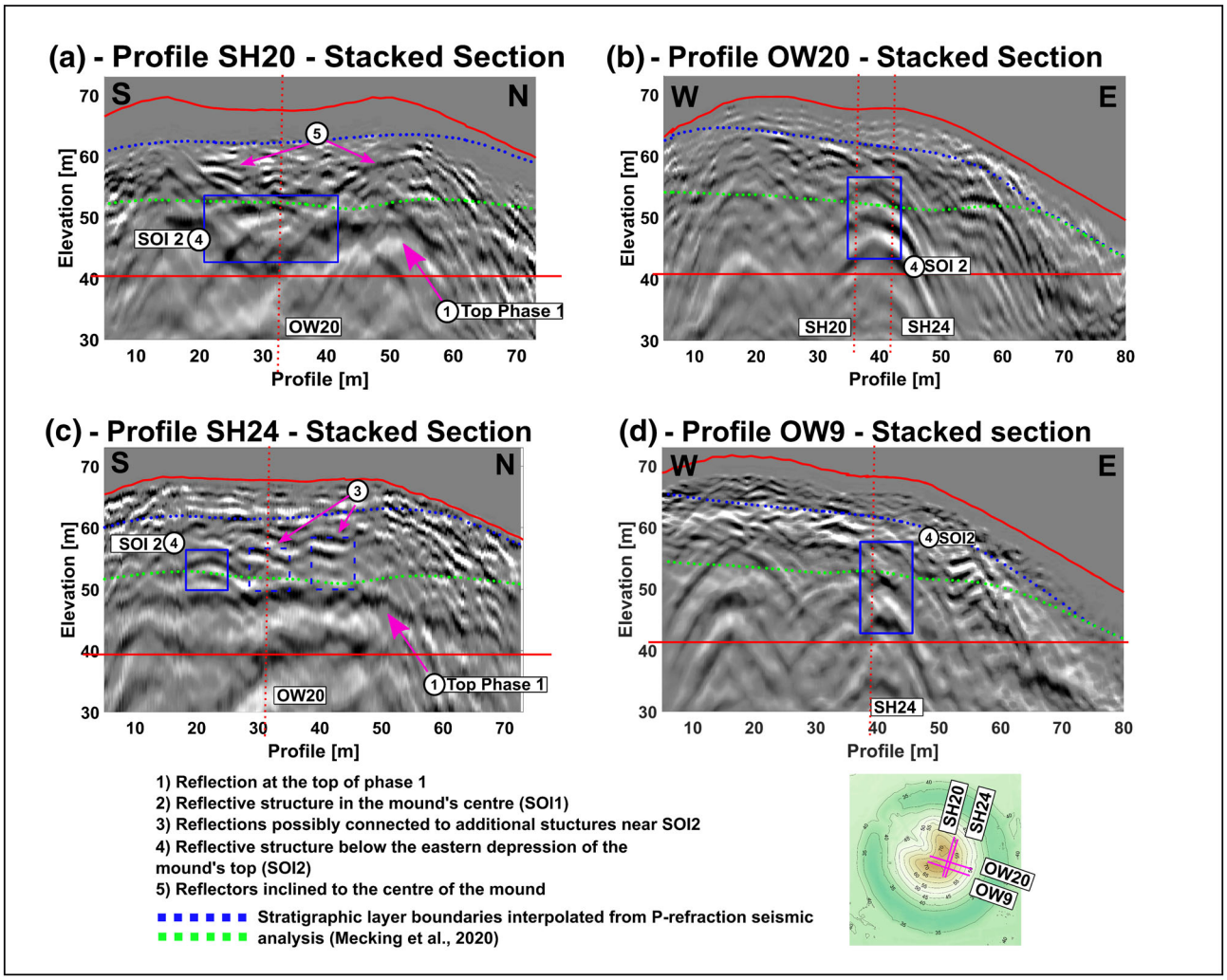


**FIGURE 7** Crossing profiles around seismic object ofinterest (SOI) 2: (a) SH20, (b) OW20, (c) SH24 and (d) OW9. SOI 2 is visible as high-amplitude diffractions on OW20 and OW9 (Marker 4) and as an elongated double reflector on SH20. (d) Profile SH24 shows diffraction hyperbolae above SOI 2 (C, Marker 3). The southern diffraction on SH24 (Marker 4) marks the southern end of SOI 2, whereas the reflections to the north might be additional constructions placed to the east of SOI 2

The CMP-stacked reflection section shows a clearly visible elongated reflector coinciding with the top of the seismic stratigraphic layer 1 (Figure 6a, green-dotted line, Marker 1), further referred to as Phase 1 reflector. It vanishes in the centre of the mound (profile metre 40) above a zone of reverberating strong-amplitude diffractions (Figure 6a, Marker 2). The diffractions migrate to distinct reflection features (Figure 6c, Marker 2) at a migration velocity of ~190 m/s. This low velocity indicates that a large volume of soil above the diffracting features is only little consolidated. In this central low-velocity zone (LVZ), some linear reflections are found that show an inclination towards the centre of the mound. They suggest subsidence in the top central part of the mound (Figure 6c, Marker 5).

The Phase 1 reflection downdips from the centre towards the northern and southern flanks. It shows strong variation in amplitude and an abrupt break off underneath the flank at about 45-m distance from the centre of the mound (Figure 6a, profile position 85). The same feature is observed on the crossing Profile OW20 also at a distance of ~40 m from the centre of the mound (Figure 6b,d; profile position 63). This lateral change is not observed by the P- or SH-refraction seismic analysis. The lateral variability of the strength of the S-wave reflections suggests that the S-wave velocity increase in Phase 1 may not primarily cause the reflection. Instead, it can be seen as an indication that the surface of Phase 1 may be a thin, consolidated layer, possibly enriched with stone packages, such as suggested by Mecking et al. (2020) based on P-wave model computations. Indeed, the existence of thin anthropogenically consolidated layers and layers of rubble was verified in other parts of the mound in several test excavations (Meinecke, 2019a; Pirson, 2016). An example is shown in Figure 1c.

Underneath the top of Phase 1, a parallel reflector of lower amplitude is found interpreted as the reflection from the basal surface of the mound. Extrapolating the height of the flat surrounding the mound into the mound interior, we determine the topographic

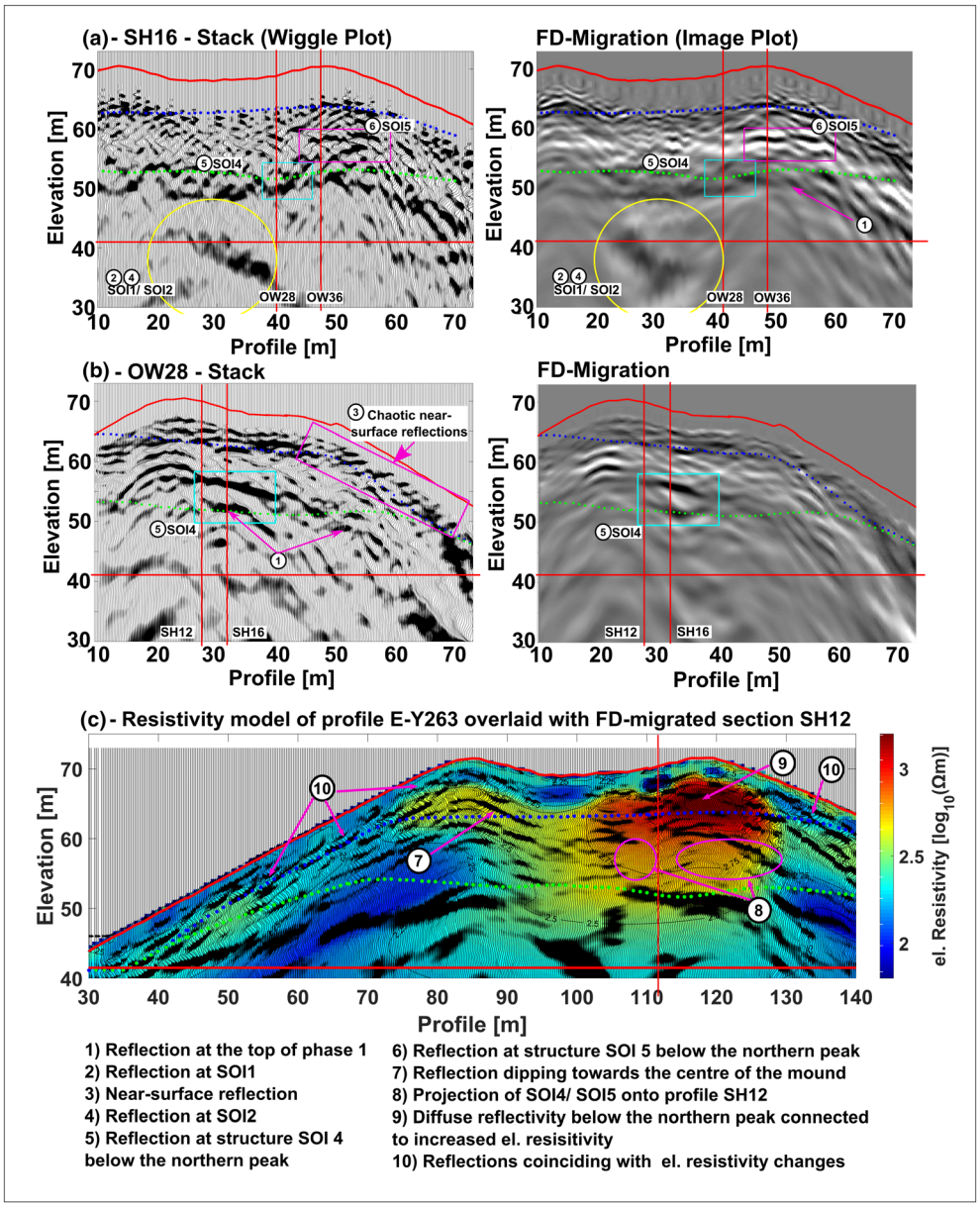


**FIGURE 8** Profiles connected to seismic object of interest (SOI) 4/SOI 5: (a) Profile SH16 showing SOI5, an elongated double reflector below the northern peak of the mound inside Phase 2 (Marker 6). (B) Profile OW28 showing an elongated double reflector situated on top of Phase 1 (Marker 5). SOI 1 and SOI 2 are visible as side reflections in the deeper part of Profile SH16 (Markers 2 and 4). The reflection at the top of Phase 1 is locally visible (Marker 1). (c) ERT Profile EY263 on migrated Profile SH12. A high-resistivity area below the northern peak of the mound stands out and correlates with scattered high-amplitudes in the seismic stack (Marker 9). This feature is possibly related to stone accumulations that might be connected to SOI 4 and 5 located to the east of the ERT profile (projection marked in pink, Marker 8). Reflectors locally fit to changes in the electrical resistivity in the flanks of the mound (Marker 10) and at the inclined reflectors below the central area of the mound (Marker 7)

height of the basal surface to 41.5 m ASL. The observed reflection is weaker than the reflection at the top of Phase 1 and occurs only locally on some profiles (Figure 6c, Marker 6). This can be explained partly by the reflection coefficients derivable from the velocity-depth distribution (Figure 2b), which are 0.25 and 0.11 for the top of Phase 1 and the base level, respectively (density contrasts neglected). The partial disappearance of the base reflection suggests that the transition between the consolidated soils of Phase 1 and the original surface soils is locally rather gradual than discontinuous. Also, despite the uniform appearance of the refraction velocity layers, internal lateral velocity variations seem to play a certain role. This is evident from some cases of reflections near the basal level, which are not aligned horizontally (Figures 8c and 6b). They may appear dipping only because of pull-up or pull-down effects of time-to-depth conversion caused by unrecognized lateral velocity variation.

### 4.1.2 | Internal reflection structure of the top seismic layer

In general, the major seismic stratigraphic units of the Yığma Tepe show a large number of small- and large-scale internal reflections above the basal surface, where the reflectivity changes its character from top to bottom. The uppermost levels (Phase 3) are dominated by chaotic small-scale scattered signals, whereas distinct reflections of larger extent appear in the levels of Phases 1 and 2. Underneath the basal surface, the seismic section shows only little reflectivity.

On all profiles, the upper 5 m below the mound surface are characterized by strong, chaotic reflections, partly eliminated next to the surface by surgical and NMO-muting, but still visible in Figure 6a (Marker 3). On some profiles, for example, OW28 (Figure 8b, Marker 3), we observe a coincidence between the depths of scatterers and

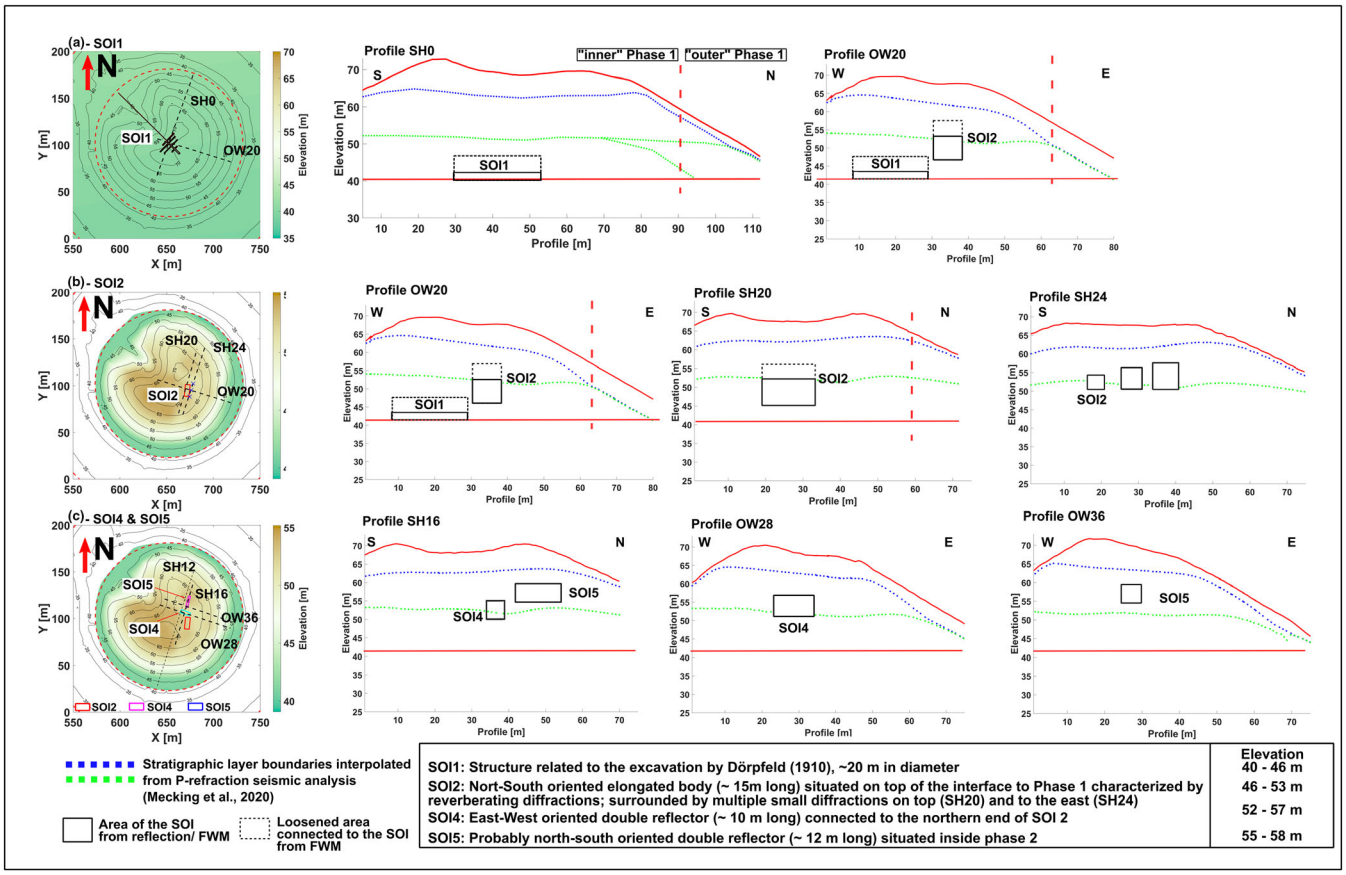


**FIGURE 9** Overview of the locations of the identified structures (a) seismic object of interest (SOI) 1, (b) SOI2 and (c) SOI 4 and SOI 5. On the left side, a map with the location of the structures is shown. The colour represents the elevation of the underlying stratigraphic layer. Contour lines show the topography for orientation; the red dotted line shows the location of the ring wall surrounding the tumulus. The location of Döprfeld's tunnels is denoted in black in (a). On the right side, seismic profiles are shown with the locations of the SOIs. The green and blue dotted lines denote the stratigraphic layer boundaries derived from P-refraction seismic (SH-refraction seismic in case of Profile SH0)

the layer boundary between Phases 2 and 3. Also, some elongated reflection elements (Figure 6c,d, Marker 7) can be associated with this transition.

Besides the chaotic arrivals, some coherent reflections are visible, which seem to form steps or narrow terraces directly below the surface (Figure 6b, Marker 5). The strong backscattering of seismic waves in the near-surface area can be explained by the aforementioned stone packages as well as radially and tangentially aligned rubble walls also found behind the ring wall and at the top of the mound (Meinecke, 2019b; Pirson, 2016).

The slopes of the Yığma Tepe were used for viticulture until the early 20th century (Meinecke, 2019a), during which the slopes were terraced with boulders. However, the steps visible in the reflection seismic extend several metres into the interior of the mound; thus, it can be assumed that the structures were built during the mound's construction to further stabilize the mound or as drainage. This was proven by new excavations 20 m behind the ring wall in 2019, where such layers were found as parts of the original stratigraphy of the mound. Therefore, Phase 3 can be regarded as a covering layer enriched by aligned stone packages serving to increase the stability of the mound and reduce erosion.

### 4.1.3 | Major localized objects at Phase 1 level

Underneath the somewhat chaotic structure of Phase 3, some distinct major reflections or diffractions are distinctly visible on crossing profiles to be discussed now in more detail.

At the centre, in the deepest part of the mound, a bundle of diffractions stands out above all other reflections, characterized by high amplitudes and comparatively long wavelengths, well recognizable on the SH0 profile (Figure 6a, Marker 2). The apex of the diffractions is located exactly at the centre of the mound near the level of the basal surface. The crossing profile OW20 intersecting Profile SH0 at the diffraction apex shows a similar pattern (Figure 6b, Marker 2; see also the perspective view in Figure 6e). The location of the corresponding reflective body coincides with the area of the tunnel system dug in the early 20th century by W. Dörpfeld (cf. Figure 1b). We hereafter refer to this diffraction structure as SOI 1. The reverberating diffractions of SOI 1 collapse to short distinct reflection elements after migration with a velocity of 190 m/s, which is rather low compared with the overall velocity of the mound. This can be explained by a complete or partial collapse of the tunnels at the mound's centre, leading to internal subsidence and decompaction of sediment near the

tunnel system. This view is supported by the inward dip of the migrated reflections. The location and extent of the Dörpfeld tunnel system are shown in Figure 9a.

The seismic reflection image alone cannot clarify the nature of the diffractive body and the cause of the reverberations. Therefore, SOI 1 is examined in more detail by forward modelling in Section 4.2.

Reflections similar to those of SOI 1 are found also on Profile OW20 (Figure 6b,d, Marker 4), located at the bottom of Phase 2 underneath the eastern part of the top area of the mound. We refer to this reflection/diffraction event as SOI 2. The reverberating diffractions have similar wavelengths as other nearby reflections but shorter than the wavelengths of the SOI 1 feature, implying a different underlying structure. On Profile SH20, crossing Profile OW20 near the diffraction apex (Figure 7a,b, Marker 4), SOI 2 shows up as a near-linear double reflector about 15 m long with multiple diffractions above. Therefore, this structure can be regarded as a 'line diffraction'—meaning a 3D reflection, which appears as an extended planar reflection on profiles parallel to strike direction and as a diffraction hyperbola along on profiles in crossline direction. The line diffraction structure is situated higher in the mound than SOI 1 and embedded into the surface of Phase 1.

The near-surface area above SOI 2, underneath the topographic depression, is characterized by comparably weak seismic signals (Figure 6b, Marker 8). This might be an indication for subsidence rather than a distortion of the topography due to digging, as this area is several metres deep, whereas the nearby recent excavation Pe17/So01 only shows disturbance of the soil up to ~0.5 m deep. The dipping reflections (Figure 7a, Marker 5) above the main reflector also suggest a partial or complete collapse of the structure underneath.

By tracking the SOI 2 reflection along all available crossing profiles, we determined its orientation to be nearly north–south. On Profile SH24, 4 m east of Profile SH20, the southern end of SOI 2 and two additional clearly separated diffractions (Figure 7c, Markers 4 and 3, respectively) supposed to be connected to SOI 2 can be recognized. The structural details of SOI 2 are investigated by numerical modelling in Section 4.2. For the orientation of SOI 2, see Figure 9b.

Two further conspicuous structures, SOI 4 and SOI 5, are found close to SOI 2 below the northern peak of the mound's top area (Figure 8a). They are located in a volume below the northern peak of the mound, characterized by strong internal reflections in Phases 2 and 3, observable for instance, on Profiles SH0 (Figure 6a) and SH12 (Figure 8c). The area is also crossed in north–south direction by an ERT profile and the coincident seismic Profile SH12 (Figure 8c). SOI4 and SOI 5 are located underneath the northern crest at about 10–15 m below the surface. This is where the ERT profile shows strongly increased electrical resistivity values reaching from about 4 m down to the top of Phase 1. In the same volume, the coinciding seismic profile shows small-scale but high-amplitude reflections comparable with those on Profile SH0. This is evident especially in the overlay figure of the ERT image and the reflection seismic section. The volume of very high electric resistivity (>1,000 Ωm, Marker 9) can be associated with large-volume stone accumulations as shown by excavations cutting through other high-resistivity anomalies at other parts of the mound (Mecking et al., 2016).

The observed clustering of strong-amplitude seismic reflectivity and high electric resistivity is unparalleled in the investigated areas of the mound. However, based on the present state of knowledge, it cannot be decided if the structure represents a funeral building or just a constructional feature. Beneath the slopes of the mound (Figure 8c, Marker 10) and below the southern crest (Marker 7) elongated reflections are found that coincide with zones of increased electrical resistivity as well. But the contrasts in both parameters are much smaller than for the cluster on top and less striking in their coincidence. The reflection seismic and geoelectric results independently show that lateral changes within the major stratigraphic layers are much more pronounced than the initial three-layered model suggests (cf. green/blue lines).

An intermediate summary is shown in Figure 9: there are four major objects of possible archaeological interest. SOI 1 is located at the bottom of construction Phase 1 and can be identified as the Dörpfeld tunnel system. It is regarded as a calibration point at the deepest part of the mound. SOI 2 is embedded into Phase 1, whereas SOI 4 and 5 are positioned on top of Phase 1, or embedded into Phase 2. SOI 4 and 5 can be associated with increased seismic reflectivity below the northern peak of the mound also visible on Profiles SH0 and SH12 and increased electric resitivities on ERT Profile EY263. SOI 1 and SOI 2 show high-amplitude reverberations, the cause of which is investigated in the following section by forward modelling.

## 4.2 | Forward modelling results

The reverberating diffractions of the SOI 1 structure are striking on all profiles across the mound's top. Concerning position and travel time, the diffraction apices correspond to the well-known location of the Dörpfeld tunnel system in the mound centre at the level of the basal surface. The dimensions of the tunnel system are well documented. Therefore, the reflection structures should be reproducible by targeted forward modelling. The most likely scenario appears to be a volume of decompacted soil comprising the collapsed tunnels and their damaged surrounding, but also open remains of the tunnels may still exist.

Forward modelling was performed to answer the following questions:

1. Is the tunnel system collapsed and, if so, can the size of the disturbed and damaged soil volume be estimated by forward modelling?
2. Are the reverberating long-wavelength diffractions of SOI 1 caused by an internal volume of unconsolidated loosened soil or by a cavity?

In contrast to SOI 1, we have no a priori information on SOI 2, but as the reflection features are similar to those of SOI 1 we can use the

experience gained from SOI 1 to reduce the number of hypothetical models and focus mainly on the following question:

3. How do SOI 1 and SOI 2 differ from each other in size and physical parameters?

We start discussing the tunnel structure, Items 1 and 2, above. For this purpose, we consider one example shot gather and compare the field data with synthetic data computed for a set of systematically varied subsurface models. To suppress ambient noise, the field data were bandpass filtered (10, 20, 80 and 100 Hz). The wavelet applied for the synthetics was adjusted by trial and error to qualitatively match the signal shape of the field data. To raise the visibility of later reflections, an analytical gain was applied to both data sets.

### 4.2.1 | Dörpfeld tunnel system (SOI 1)

For investigating SOI 1 by wavefield modelling, we selected exemplary shot gathers from Profile SH0 (Figure 6a) because this profile crosses the apex of the SOI 1 diffraction bundle (Figure 6e). Five different hypothetical model variants are shown to illustrate the process of model construction and to support the most appropriate model in comparison with plausible, but less well-fitting alternatives (Figures 10a–e, top).

The dimensions of the objects inserted into the background model were chosen based on the historical records of Dörpfeld (1910). A rectangular area of 20-m width and 5-m height above the basal surface of the mound is filled with a gradient velocity structure decreasing to 200 m/s at the base (Figure 10b,d,e, top). It represents a collapsed tunnel system with a damage zone of decompacted soil above it. Physically, it is represented by decreased shear wave velocities compared with the surroundings, where the minimum S-wave velocity of ∼200 m/s corresponds to the velocity found at the mound's surface. The damage zone above the collapsed tunnels is modelled by gradually extending the minimum velocity upward into the undisturbed zone using a velocity gradient.

It is also known that a well or shaft was dug into the basal surface exactly at the centre of the mound (Dörpfeld, 1910), but it is unknown whether it was refilled before the tunnel was abandoned. This is implemented in some of the models as a second, smaller area of 5 × 3 m cross section below the collapsed tunnel system. Two cases are investigated: an air-filled cavity (Figure 10d) and a cavity filled with loose sediments realized as a second gradient zone with velocities decreasing downwards from 130 to 80 m/s (Figure 10d,e, top, respectively).

In the following, we first consider the synthetic seismograms generated by the single model components: the background model (Figure 10a), the background model plus collapsed tunnel system and the background model plus a loosely filled shaft (Figure 10b,c, respectively). Then, both collapsed tunnel and shaft are modelled in

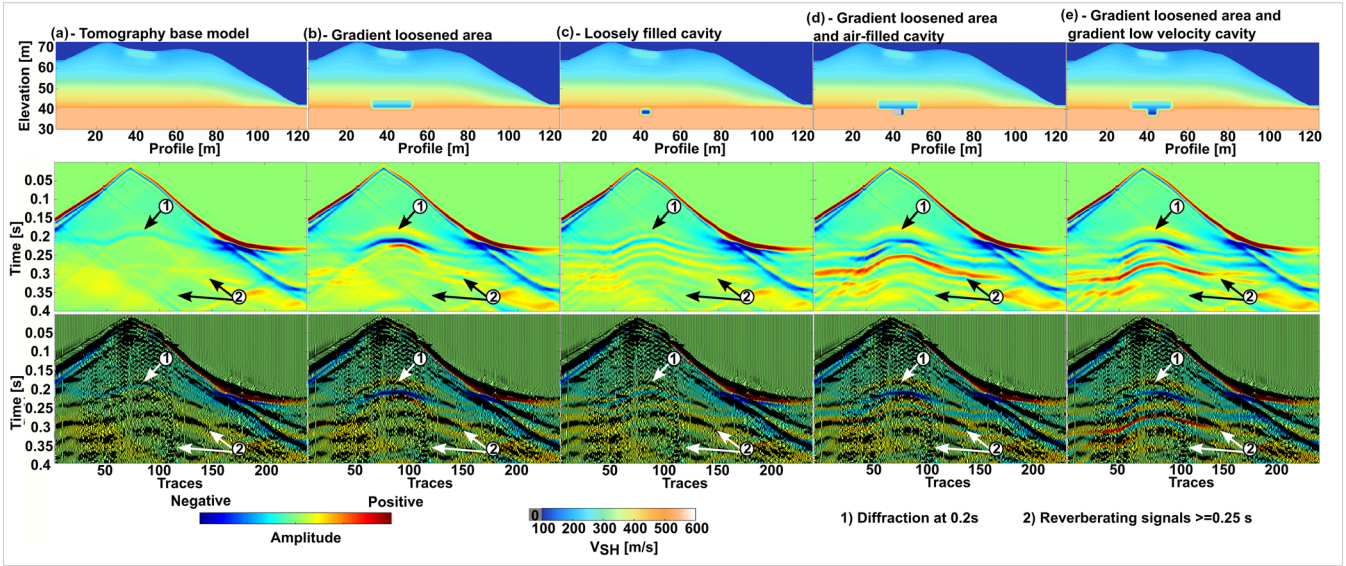


**FIGURE 10** SH-viscoelastic forward modelling of one exemplary shot on profile SH0 for (a) the tomographic base model, (b) Model (A) with a low-velocity area with a negative velocity gradient with depth (360–200 m/s); (c) Model (A) with a loosely filled cavity ($V_{SH}$ = 70 m/s). Calculated data of one shot are imaged in colour (centre, bottom) and the measured data is overlaid as black wiggle (bottom). All three models generate well-fitting first-arrival times (Marker 3); Models A and B achieve the first reflection hyperbola (Marker 1), but all fail in fitting the waveform, offset behaviour of the diffraction and successive diffraction fitting. (d) Combination of both volumes with an air-filled cavity (depicted grey; D) and a negative gradient (E, 130–50 m/s). In the centre, the modelled shot is shown. In the bottom, the modelled shot is overlaid with the respective data as a wiggle plot. The forward modelled shot on (d) differs only gradually from the shot at Model E. Some additional diffractions are visible at Marker 2. Thus model E fits the measured data best in waveform, offset behaviour of the diffraction branches and reverberation of the diffractions

combination, once with an air-filled well and once with a loosely filled well (Figure 10d,e, respectively).

In comparing the models, particular attention has to be paid to the adaptation of the first high-amplitude reflection at 0.2 s (Figure 10, Marker 1) originating from the reflection at the top of the loosened area and the following long-wave reverberations at ≥0.25 s (Figure 10, Marker 2), originating from the low-velocity anomalies in the centre of the mound at the level of the basal surface (see arrows in Figure 10).

The synthetic seismograms of the background model match the measured first arrival well, but almost no reflections occur due to the smoothness of the model (Figure 10a). The collapsed tunnel system alone is capable to reproduce the observed top reflection at 0.2 s (Figure 10b, Marker 1) but fails with the reverberations (Figure 10b, Marker 2). For creating reverberations, it is necessary to insert a cavity (air-filled or loosely filled, $V_{SH} \leq 100$ m/s) into the background model at the basal surface (Figure 10c). However, still a mismatch remains concerning the travel times of the reverberating phases in the succession of the reverberations and wavelength being shorter than observed. Adding the LVZ of the collapsed tunnel system to the cavity model can compensate for this (Figure 10d,e).

The best match with the measured data was achieved by combining the collapsed tunnel LVZ with the loosely filled shaft model (Figure 10e). The corresponding synthetic seismograms reproduce the observed reflections in all regards: travel times, relative amplitudes, amplitude decay with offset and apparent wavelengths. A closer look at the low-amplitude signals shows that the reverberating diffractions modelled well even down to 0.35 s. To visualize the process creating these signals, snapshots of the forward-modelled wavefield are shown in Figure C1. The LVZ not only reflects the incoming wave at the surface but also admits transmission into the interior where the wave bounces back and forth, sending out secondary 'pulses' in time intervals depending on the size and the velocity inside the LVZ. The remarkably long wavelength compared with the more shallow reflections above is caused by the velocity structure inside the LVZ.

An air-filled cavity, in contrast to a loosely filled one, also creates a comparable good result, differing only in small details. Thus, it remains unclear whether there is still an air-filled area inside the scattering object.

In summary, we find that the dominant seismic reflections on the SH0 profile can be reproduced by two adjacent low-velocity volumes in the centre of the mound, the extent of which matches the Dörpfeld records of the tunnel system. Due to the height of the loosening zone and the decrease in $V_{SH}$ with depth, we assume that the tunnel system has collapsed. The gradual decrease of $V_{SH}$ with depth into the collapsed tunnel volume is necessary for fitting the observed seismograms because a velocity discontinuity would produce a strong reflection at the top of the loosened volume and additional internal multiples, a feature which is not observed (cf. Figure C2c). The very low velocities in the shaft suggest that the shaft was even less densely filled with soil by the collapse than the tunnels or that it stayed partly air filled.

A more general conclusion from Figure 10 is that the diffraction pattern as a whole, including its complicated field of multiples, is a very sensitive first-order distinctive feature regarding the causative structure behind. Other distinctive features are changes in the waveforms of particular phases. However, these are more difficult to identify visually in field data. The most reliable way to evaluate this more subtle information is through FWI, which we applied to the data in a companion paper (Mecking et al., 2021), which confirmed our interpretation.

From Dörpfeld's records (Dörpfeld, 1910; Figure 2), the well dug in the centre of the mound can be estimated to be about 2 m in diameter and 2 m deep. The best-fitting forward models, however, were achieved for a well of 5 m in diameter and 3 m in depth. However, smaller wells generate seismograms that do not match the observed reverberations, especially the 0.25-s phase, in amplitude and time (Figure C2d). It is unlikely that Dörpfeld did not document the enlargement of the tunnel in the centre of the mound, as his drawings and records are very accurate overall. However, it may be possible that the tunnel was opened again after the end of the excavation by another party and further excavations might have been carried out.

### 4.2.2 | Construction in Phase I (SOI 2)

Based on the experience gained in modelling SOI 1, SOI 2 was investigated according to the same scheme. For forward modelling, we selected one shot gather of Profile OW20 (Figure 6b,d), which crosses the structure at its centre orthogonally to the strike direction.

Again, we show synthetic seismograms for the background model and four different model variants (Figures 11). In analysing the seismograms, special attention has to be paid to the succession of the diffractions from 0.15 s onwards. (e.g., Figure 11, Markers 1–3).

To fit the first arrivals, a thin high-velocity layer has to be added to the background model at the top of the mound at about 1 m below the surface (Figure 11a). In the western section of the profile, the HVZ known from Profile SH0 was also added to improve the fitting of the first arrivals. Further slight adjustments had to be applied in the slopes and to the course of the layers to model the loosened soil of the uppermost metres and to improve the fit of the first arriving phases (Figure 11a).

As we observed in modelling SOI 1, both a low-velocity area and an air-filled cavity can produce reverberating diffractions. There is no a priori information for the structure examined on this profile apart from the CMP section. To reduce the number of possible models, however, the following boundary conditions can be established:

1. The signals are similar to the signals observed at SOI 1, caused by areas of loosened material.
2. Cavities can produce reverberating signals with short wavelengths and weak amplitude.
3. The diffractions migrate to local reflection elements, limiting the location of the diffracting structures (Figure 6d, Marker 4)
4. The slightly overmigrated diffraction branches of the migrated section indicate zones of locally reduced velocity above SOI 2 (Figure 6d, Marker 4). The local traveltime shift of the diffraction

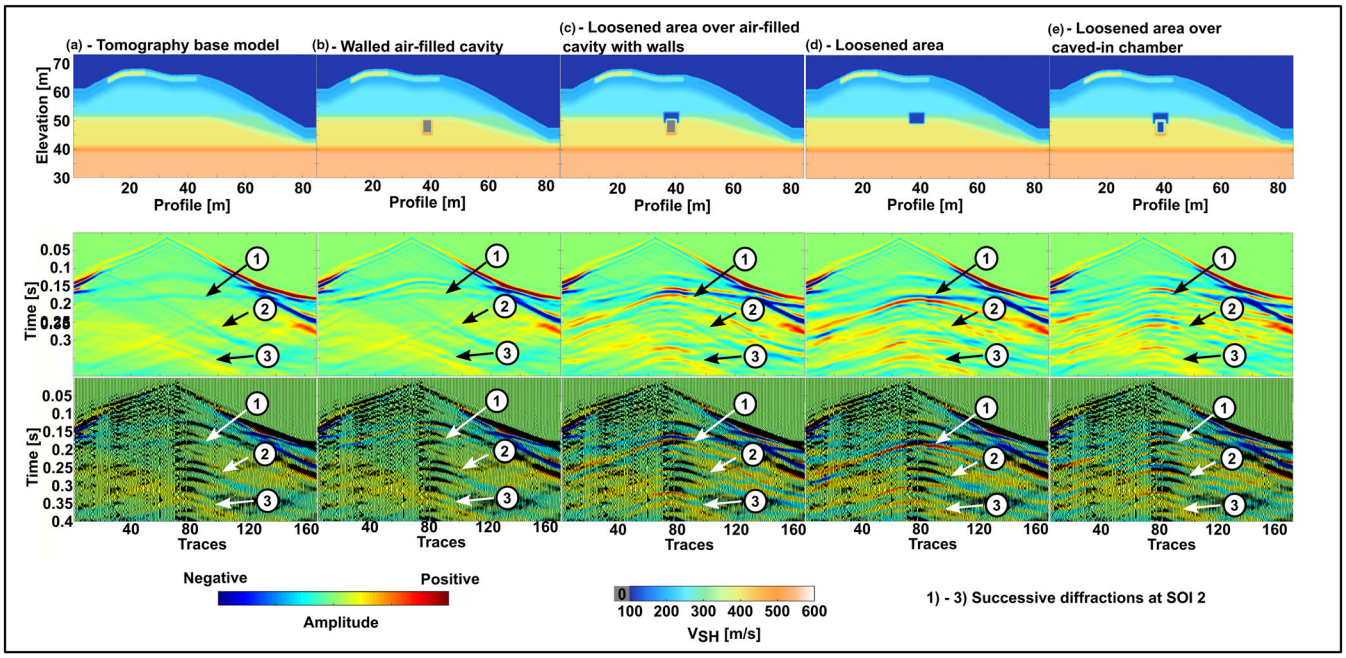


**FIGURE 11** SH-viscoelastic forward modelling of one exemplary shot on Profile OW20. (a) The tomographic base model, (b) a walled air-filled cavity (depicted grey) and (c) a loosened area (5.5 m × 4 m, $V_{SH}$ = 110 m/s) above an air-filled cavity (4 m × 2.5 m, $V_{SH}$ = 0 m/s) surrounded by walls. Centre: the modelled shot bottom: the modelled shot is overlaid with the respective data as a wiggle plot. Modelling of the tomographic model A can only explain the first arriving waves. (b) A walled air-filled cavity creates diffractions of weak amplitude which do not resemble the real data. (c) The low-velocity zone above the air-filled cavity leads to the creation of multiple diffractions but the reverberating diffractions (Marker 2) are too weak. (d) Volume of decompacted soil (5.5 × 4 m, $V_{SH}$ = 110 m/s) and (e) volume of decompacted soil in combination with a walled second volume of decompacted soil representing a collapsed chamber or access tunnel (3 × 2.5 m, $V_{SH}$ = 100 m/s, E). The signals of Model E fit the measured signals best in succession of the reverberating diffractions, the dip of the traveltime branches and the location of the diffraction apices, making a collapsed building structure the most likely scenario

branches and the reduced overmigration to the right side of the diffracting structure indicates that the LVZ above ends abruptly.

The signal an air-filled walled cavity creates is shown in Figure 11b. The signals arrive in faster succession showing relatively weak amplitudes compared with the measured data. Therefore, a thick-walled brick burial chamber would only be recognizable by the reflection from its roof and not distinguishable from the reflection at a solid body. This means that on the one hand, intact burial chambers cannot be identified uniquely by forward modelling and on the other, SOI 2 must be a LVZ of similar nature as SOI 1.

Therefore, a LVZ was inserted directly above the overmigrated diffractions (Figure 11d, top). Its size was adjusted to match the reflections at SOI 2 (Figure 6d). The comparison of the modelled and measured data (Figure 11d, bottom) shows partly well-fitting diffraction branches, but, overall, the modelled sequence of diffractions is vertically less dense than observed, especially the strong double diffraction at Marker 2, and the diffractions appear flatter as observed in the measured data.

A second, smaller, LVZ of ~2.5 × 4 m was inserted underneath, separated by a 'roof' from the LVZ above and surrounded by walls. This model (Figure 11e) shows the best match with the measured data for most of the successive diffractions, especially the strong diffractions at Marker 2, and their offset behaviour. Even the slightly asymmetric diffraction apices (i.e., Marker 2) are reproduced well.

This model stands for a collapsed walled volume that is filled with sediment resulting from the collapse, from which the overlying zone of decompacted soil results. It fits the reflections in section OW20 (Figure 6d). An air-filled cavity (Figure 11c) produces less fitting diffractions and a downward shift of the strong double diffraction at Marker 2.

## 5 | DISCUSSION

SH-wave reflection imaging has shown that the Yığma Tepe shows strong heterogeneity above the natural soil at the basal surface. For the differentiation of properties of the reflecting structures, forward modelling made an important contribution. In the following, the results of both methods will be reviewed and discussed in the archaeological context, considering the seismic stratigraphic structure of the mound (Mecking et al., 2020) and archaeological excavations (Dörpfeld, 1910; Meinecke, 2019a; Pirson, 2016).

As SH-wave reflection imaging is a rarely applied tool of archaeological prospecting, we also discuss to what extent it met the previously defined prospection requirements, leading to the following questions:

1. How do combinations of SH-wave seismic and P-wave seismic complement each other?
2. What are the advantages and disadvantages using shear wave seismic? Did they fulfil the expectations placed on them? What perspectives exist for further improving the method?
3. How does the seismic investigation of the Yığma Tepe compare with other geophysical exploration methods at burial mounds?
4. How are the SOIs to be assessed based on their location and extension, and how can they be compared with the finds of other burial mounds?

## 5.1 | How do combinations of SH-wave seismic and P-wave-seismic complement each other?

By means of P-wave measurements, three layers of different velocities, each 10 m thick, were distinguished representing three construction phases (Figure 2a; Mecking et al., 2020). Based on previously defined layers from P-wave measurements, a similar, fitting model was created from the SH first arrivals (Figure 2b). The $V_P/V_S$-ratio shows a constant value of 2 above the basal surface of the mound and increases to 2.4 underneath.

The sharp, high-amplitude reflections at the surface of Phase 1 support the assumption from refraction seismic that the layer transition from Phases 1 to 2 is a sharp boundary. This might tentatively be explained by artificial solidification, for example, by finer-graded material or gravel layers as found in excavations on the mound (Meinecke, 2019a; Pirson, 2016).

The reflection seismic also shows that Phase 1 is not laterally homogeneous but seems to be subdivided into an inner mound with a radius of about 45–50 m and an outer ring with a thickness of 30–35 m (Figure 6). Because the reflection is very strong only on the inner segment of Phase 1, this would support the thesis of a thin, hardened layer deposited on Phase 1. The outer ring would then consist of the same fill material as the inner ring but not hardened at the surface. The reflection at the basal surface of the mound (Figure 6, Marker 6) is weak compared with the Phase 1 reflection, further supporting the thesis of an artificially hardened top of Phase 1.

In addition, the three phases differ in their reflection patterns. Phase 1 shows no internal reflections, apart from the diffractions caused by the collapsed Dörpfeld tunnel, whereas major seismic features were identified in Phase 2, partly lying on the surface of Phase 1 or embedded therein. In contrast, Phase 3 is characterized by dense patterns of small-scale features that cause chaotic scattering effects.

## 5.2 | What are the advantages and disadvantages of using shear wave seismic? Did they fulfil the expectations placed on them? What perspectives exist for further improving the method?

The structure of the entire mound can be investigated by means of SH reflection seismic. Layer boundaries, as well as small-scale structures, were identified. They do not always agree exactly with previous information obtained from P-wave refraction seismic. This is because P-wave traveltime tomography has a much lower lateral resolution (in this case ~15 m; Mecking et al., 2020) than SH-wave reflection seismics. To demonstrate the resolution of the reflection seismics, we calculated a resolution test via exploding reflector model. For simplification, we used a homogeneous mound model with the RMS velocity at the base level (260 m/s) and an underlying homogeneous half-space (500 m/s) (Figure A1). Three bodies (2 rectangular structures with 3- and 5-m side lengths and a wedge with 0- to 4-m height) with contrasting velocity (100 m/s) are to be resolved. It shows that after migration, the upper and lower edges of the wedge can be separated at 1.2-m wedge height (Figure A1b). Although the upper/lower edge of the 5-m rectangle is well resolved, the limit of resolution at the 3-m rectangle is shown by the not accurately resolved upper/lower edge (Figure A1c). Based on a well-defined velocity model, this results in a resolution of a few metres.

This means that the problems caused by the limitations of penetration depth and structural resolution, which restrict the applicability of ground radar, geoelectric and magnetics, can be overcome by shear wave seismics and that archaeologically relevant structures such as stone-set buildings or cavities can be detected at decametre depth. Near the basal surface the resolution drops due to decreasing signal frequency and increasing shear wave velocities (cf. Section 3.1). However, the synthetic computations (Figure 10) show that the shear wave field is still sensitive enough for discriminating different model scenarios. At the same time, the high resolution and sensitivity of SH-wave sounding are also one of its problems. Structures of archaeological interest have to be distinguished from the heterogeneity of stone interspersed soils piled up in patchy layers. It should also be considered that the seismic wave propagates three-dimensionally in the subsurface, whereas our survey was recorded in 2D along linear profiles. The separation and evaluation of side scatterers are required in the survey design if the data cannot be recorded in full 3D for logistic or economic reasons.

In the present study, we applied cross profiling to identify the location of local scatterers and to assess the extent and importance of the reflecting bodies. However, despite a profile spacing of 4 m in both directions, interpretation of 3D structures remained difficult due to the small-scale heterogeneity of background soil. Therefore, 'true' dense-grid 3D sounding is desirable for future measurements with similar objectives. In addition, three-component geophones should be used to enable the separation P-/SV and SH phases by directional vector field analysis and differential operations (Wölz et al., 2009; Wölz & Rabbel, 2005).

The forward modelling has shown even small cavities produce a clearly distinguishable signal compared with equal-sized solid bodies, not producing reverberating diffractions. Modelling has also shown that even a very small cavity of wavelength dimension in the centre of the Dörpfeld structure >30-m depth still produces a clearly distinguishable signal (Figure C2d). Thus, shear wave seismic is very well suited for detecting cavities in sediments, a capability that can also be

useful apart from archaeological questions, for example, in the geotechnical sector where cavities often pose a threat to modern building structures. We would like to emphasize that the diffraction patterns are unique for cavities and LVZs in sediments. Their shape and sequence depends on the dimensioning and seismic velocity of the LVZ, because the multiples are largely caused by internal reflections.

Thus, with forward modelling, the size and characteristics of the low-velocity structures underlying the seismic signals can be narrowed down. Still, some uncertainties remain regarding their exact depths and structural details because of the general limitations in resolution. Especially for SOI 1, covered by ~20-m-thick sediment, the assumed mean velocity above the structure is crucial for its placement, size and internal velocity. This central volume is not only characterized by an HVZ directly below its surface but also by a chaotic reflection pattern with dipping reflecting horizons and an interruption in the Phase 1 reflection (Figure 6a,c). This suggests that the velocity structure is more complicated on a small scale than assumed in the background model, especially towards the flanks of the mound. Also, the tunnel system with its drillings is certainly more complex than modelled at scales below the wavelength. To clarify this in more detail, 'true' 3D data acquisition in a narrow grid and corresponding modelling has to be performed.

In the case of SOI 2, the horizontal position is clearly determined by reflection seismics and comparative modelling. However, due to the uniformly reverberating diffractions, errors in the vertical position of the two structures may occur. The diffractions are composed of primary top reflections, internal reflections and multiples. It also has to be considered that a vertical shift of SOI 2 by a few metres can lead to a similar result (Figure C3d).

### 5.3 | How does the seismic investigation of the Yığma Tepe compare with other geophysical exploration methods at burial mounds?

To our knowledge, the present study is the first to apply SH-reflection sounding to the exploration of a monumental burial mound. Lütjen and Utecht (1991) used P-wave reflection profiling among other methods at the Nemrut Dağ in Eastern Turkey. The results were used to enhance the information from refraction seismic and GPR. Due to the higher P-wave velocities, the resolution is much lower than in our shear wave study and apart from stratigraphic layer boundaries no additional structures were identified. A multilayered hill over partially weathered bedrock with variable topography was reconstructed by refraction seismics. Step-like constructions were identified in the slopes. No burial constructions were identified by geophysical means.

On smaller burial mounds, GPR reflection imaging was successfully applied to locate internal buildings and burials (e.g., Kamei et al., 2000; Persson & Olofsson, 2004). At very shallow depths, for example, on very flat burial mounds or in the flanks at the edges of mounds, grave chambers were also directly identified through ERT (Papadopoulos et al., 2010).

At Kastas tumulus in Greece, geoelectric and P-wave refraction tomography were mainly used to identify larger disturbed soil volumes around burial structures associated with electric resistivity or velocity anomalies, such as access tunnels or excavation pits (e.g., Polymenakos et al., 2004; Tsokas et al., 2018).

While near-surface structures can be imaged faster and on a denser grid by GPR and ERT, the shear wave seismic adds the high resolution at an increased depth, which cannot be obtained by any other geophysical method. Combining these methods is thus advisable when dealing with archaeological targets from the surface up to several tens of metres depth.

### 5.4 | How are the SOIs to be assessed based on their location and extension, and how can they be compared with the finds on other burial mounds?

The SOI 1 structure, attributed to the collapsed Dörpfeld tunnel system, provides a certain methodological calibration, but it is clearly not of primary archaeological interest. In contrast, SOI 2 can be regarded as a major archaeological feature. Its location at ~4–5 m above the basal surface, its elongated north–south-oriented shape and the structures around it (cf. Section 4.1.3) make it the main feature of interest found by reflection seismic. The results of the forward modelling (Figure 11e) suggest it was originally a walled cavity, whose collapse created an area of decompacted soil above it and lies directly under the surface of Phase 1. Although the exact meaning of SOI 2 is not clear, judging by its size and proportions, it might represent a potential disturbed architectural tomb structure.

The position of SOI 2 is displaced by about 20 m to the East with respect to the geometric centre of the Yığma Tepe. A visual connection between the Yığma Tepe, the Sanctuary of Athena and especially the Great Altar on the city hill of Pergamon over a distance of 3 km is assumed. Interestingly, the prolonged axis from the western side of the Great Altar does not pass the geometric centre of the mound but approximately SOI 2, which is roughly oriented along this axis (Pirson & Ludwig, n.d.).

The location of SOI 2 coincides with the positions of known grave chambers of smaller burial mounds in the Pergamon area, such as the Taşdam Tepe (Stappmanns, 2012), Ilyas Tepe (Pirson, 2011) and Seç Tepe (Kasper, 1966). The distance (20 m) and direction (East) of the offset of SOI 2 are surprisingly similar to what has been found at Mal Tepe burial mound in Pergamon from the Roman period. It has an accessible dromos and grave chambers lying 21 m east of the geometric centre of the mound (Dörpfeld, 1907). However, dromos and grave chambers of the Mal Tepe are at its basal surface, whereas the location of SOI 2 at ~4–5 m over the ancient surface appears unusual for a possible primary grave complex. Frequently, grave chambers are found on the original surface level or, even more common, set in pits dug into the natural soil. This applies especially to the barrel-vaulted Hellenistic chamber tombs of the so-called Macedonian type (Mangoldt, 2012). In Pergamon, this type is found at the Hellenistic tumulus on the Ilyastepe (Pirson, 2011) or in the first century BC

tumulus near the Asklepieion in Pergamon (Ziegenaus, 1966). Sometimes the whole chamber is lying even below the ancient surface as in the Hellenistic Naip tumulus of Southeastern Thrace (Delemen, 2006) or the older Tumulus at Kourinos in Greece (Mangoldt, 2012). Dörpfeld had already expected a walled grave chamber would lie eccentrically on the ancient surface and would not be found higher in the embankment because the freshly deposited earth would not be stable enough to support the weight of such an architectural structure. He concluded only a smaller sarcophagus might be placed in such a stratigraphic position (Dörpfeld, 1910). In some archaic tumuli of ancient Lydia (district Manisa) like Demirağ and Akpınar D, it was observed that sarcophagi were set into the upper layers of older tumuli covering primary architectural tomb complexes (Roosevelt, 2003). In the tumulus 'Kizöldün' in the Troad, a sarcophagus has been found in eccentric position only slightly below the actual surface of the mound that covered an about 50-years older sarcophagus burial placed in its centre (Rose, 2014).

Therefore, SOI 2 might represent a secondary burial, but its dimensions and characteristics point to a larger built feature. Considering that it was set into an older mound represented by Phase 1, the fill might have been naturally compacted as suggested by the seismic P-velocities and could have supported such heavier structures. Only in few cases grave chambers have been found at higher levels inside a burial mounds. A prominent example is the Karakuş tumulus in East Anatolia where evidence of a chamber was found 8 m over ground in an eccentric position as well (Dörner, 1969/1970). However, the Karakuş tumulus is constructed on a rather steep hillslope not comparable with the topographic situation of the Yığma Tepe. Another example might be the Askertepe tumulus near Tekirdağ in ancient Thrace (Northern Turkey) where the architectural tomb complex of the second half of the fourth century BC seems to lie ~3–4 m high in the mound's fill in an eccentric position, but the excavation report does not mention this explicitly (Yildirim, 2010). In both cases, no other burial structures on the ancient basal surface are known as the mounds are not completely excavated. In Bulgaria, architectural complexes of Hellenistic time belonging to Ancient Thrace as well were found 1.5 m over the ancient ground in the Slavchova Tumulus near Rozovo and Sarafova tumulus near Kazanlak (Kitov, 2003). In these completely excavated tumuli, Kitov observed that an artificial mound had been piled up in a first construction stage and later some earth had been removed for the construction of the chamber. In the Sarafova tumulus, the earth had not been consolidated enough and the walls of the grave chamber sagged—as expected by Dörpfeld (1910). In the same region, more temple-like architectural structures have been recorded in the upper fill about 3 m over the ancient surface in the Ploskata Tumulus or at even 8-m height in the Donkova–Tumulus near Shipka (Dimitrova, 2007). But such structures have never been observed in Hellenistic tumuli in Turkey and the region of Pergamon.

Therefore, these examples might not be applicable. SOI 2 could represent a primary structure, as there is no evidence in the geophysical data for a primary burial on the base layer inside Phase 1. However, tests on intact walled air-filled cavities (Figure 11b) have shown that they would produce only weak seismic signals and would not be as clearly identifiable as found in the SH-wave survey. This means that an intact burial chamber may produce less significant seismic signals than a caved-in structure and might, under unfavourable conditions, not be distinguishable from a heterogeneous background.

As SOI 4 and 5 even appeared in a higher stratigraphic position and might have been constructed on the surface of Phase 1, a multiphased construction of the Yığma Tepe seems likely and is supported by the stratigraphy derived from reflection and refraction seismic suggesting a subdivision of Phase 1 into an inner part with a hardened surface and an outer part. Additionally, Dörpfeld recorded a hardened core mound of about 30 m in diametre during the tunnel construction. However, without archaeological findings proving a longer construction time and other archaeological features, such as an older inner burial or an inner crepis wall, the construction phases could have been realized in quick succession without longer breaks as well (Mecking et al., 2020).

Although SOI 2 might represent an architectural grave complex that was set in a pre-existing mound or in the process of its construction, no definite conclusion can be drawn based on the geophysical and archaeological evidence available.

Our reflection seismic survey of the Yığma Tepe is by no means complete. Especially in the slopes and near the ring wall where the topography is the steepest, only few profiles have been measured. Main burial complexes might exist, especially in the outer ring of Phase 1, which we hardly covered at all. Our measurements showed that the identification of burial structures is possible, but a dense regular grid would be necessary to achieve this.

## 6 | CONCLUSION

We investigated the interior of the monumental burial mound Yığma Tepe using SH-wave reflection imaging and traveltime tomography. The results were evaluated using numerical wavefield modelling and information from historic and recent archaeological excavations. They lead to the following conclusions:

The Yığma Tepe can be subdivided into three stratigraphic layers representing different construction phases of each about 10-m thickness. The top layer, Phase 3, is most heterogeneous. It contains a lot of scattering objects identified as a net of stone settings in test excavations. The stone settings are thought to stabilize the surface of the mound.

In stratigraphic Phase 2, three SOI were detected. They are located on and above the top of Phase 1 and under the northern summit but at different depth levels. It is unclear whether they are connected with each other.

The largest of these SOIs is a north–south-oriented structure of about 15-m length and 4-m width. SH-viscoelastic forward modelling showed that it likely consists of a collapsed walled cavity with a zone of loosened soil above. The top of this structure is found about 13 m below a depression at the top of the mound,

whereas the floor of the assumed structure is about 5 m above the basal level of the mound. The archaeological significance and interpretation of these structures remains unclear, because they lack similarity with other burial mounds. In particular, there is no known case of main burial construction placed on a clearly elevated building phase.

The deepest layer, Phase 1, is the most consolidated layer. Its surface is locally compacted by overlying sediments or deposition of pebble layers. The SH-wave reflection sections suggest a subdivision into an inner Phase 1 with a radius of 40–50 m and an outer Phase 1. We found the collapsed remains of a tunnel system and a shaft at the basal surface that had been dug into the mound at the beginning of the 20th century. This finding can be regarded as a calibration of the S-wave sounding. The tunnel collapse created a damage zone of decreased S-wave velocity extending up to Phase 2.

Methodologically, we were able to show shear wave reflection seismic can detect metre-scale archaeological structures at 10-m-scale depth. Our numerical modelling results show we can distinguish between different cavity fillings by seismic forward modelling, thus making it possible to distinguish solid bodies from loosened soil and cavities.

## ACKNOWLEDGEMENTS

We thank the German Archaeological Institut (DAI) for supporting this project and the Deutsche Forschungsgemeinschaft (DFG) (grant number: 246601872, project number: PI 404/6-1) and the Agence nationale de la recherche (ANR) for funding our work. The geophysical surveys between 2014 and 2017 were part of the archaeological project NekroPergEol (PIs Prof. Felix Pirson, DAI Istanbul, and Prof. Stéphane Verger, Archéologie et Philologie d'Orient et d'Occident (AOROC), which deals with the context of funerary customs and society in the Aeolis at Hellenistic times.

Thanks to all students from Kiel University and Kocaeli University who participated in the field campaigns 2014–2018. Also, thanks to the Geophysical Instrument Pool of the Deutsches Geoforschungszentrum Potsdam (GIPP), Umweltforschungszentrum Leipzig (UFZ), the University of Hamburg and the University of Karlsruhe for lending us geophysical equipment.

Finally, thanks to the Ministry of Culture and Tourism of the Republic of Turkey, the Head Office for Cultural Monuments and Museum for the work permissions. Thanks to the representatives of the Ministry as well as to the management of the Museum of Bergama for their support.

Last but not least, we are greateful to Peter Lanzarone and two anonymous reviewers for their constructive critique that helped to improve our article.

## CONFLICT OF INTEREST

The authors have declared no conflict of interest.

## DATA AVAILABILITY STATEMENT

The data that support the findings of this study are available from the corresponding author upon reasonable request.

## ORCID

*Rebekka Mecking* https://orcid.org/0000-0002-2651-2077

## REFERENCES

Delemen, I. (2006). An unplundered chamber tomb on Ganos Mountain in southeastern Thrace. *American Journal of Archaeology*, *110*(2), 251–273. https://doi.org/10.3764/aja.110.2.251

Dimitrova, D. (2007). The temple in Horizont Tumulus in Central Bulgaria. In A. Iakovidou (Ed.), *Thrace in the Graeco-Roman world, proceedings of the tenth international congress of Thracology* (pp. 135–139). National Hellenic Research Foundation: Athens.

Dix, C. H. (1955). Seismic velocities from surface measurements. *Geophysics*, *20*, 68–86. https://doi.org/10.1190/1.1438126

Dörner, F. K. (1969/1970). Kommagene - Forschungsarbeiten von 1967 bis 1969. *Istanbuler Mitteilungen*, *19/20*, 273.

Dörpfeld, W. (1907). Die Arbeiten zu Pergamon 1904-1905. I. Die Bauwerke. *Athener Mitteilungen*, *32*, 161–240.

Dörpfeld, W. (1910). Die Arbeiten zu Pergamon 1908-1909 I. Die Bauwerke. *Athener Mitteilungen*, *35*, 346–400.

Forte, E., & Pipan, M. (2008). Integrated seismic tomography and ground-penetrating radar (GPR) for the high-resolution study of burial mounds (tumuli). *Journal of Archaeological Science*, *35*, 2614–2623. https://doi.org/10.1016/j.jas.2008.04.024

Hunter, J. A., Pullan, S. E., Burns, R. A., Gagne, R. M., & Good, R. L. (1984). Shallow seismic reflection mapping of the overburden-bedrock interface with the engineering seismography, some simple techniques. *Geophysics*, *49*(8), 1381–1385. https://doi.org/10.1190/1.1441766

Inazaki, T. (2006). Relationship between S-Wave velocities and geotechnical properties of alluvial sediments. *Symposium on the Application of Geophysics to Engineering and Environmental Problems 2006*. Environmental & Engineering Geophysical Society, 1296–1303.

Kamei, H., Marukawa, Y., Kudo, H., Nishimura, Y., & Nakai, M. (2000). Geophysical survey of Hirui-Otsuka Mounded Tomb in Ogaki, Japan. *Archaeological Prospection*, *7*, 225–230. https://doi.org/10.1002/1099-0763(200012)7:4<225::AID-ARP136>3.0.CO;2-C

Kasper, S. (1966). Der Grabtumulus Sec-Tepe bei Elaia. *Archäologischer Anzeiger*, *81*, 477–478.

Kelp, U. (2014). The Necropolis of Pergamon. In A. S. Felix Pirson (Ed.), *Pergamon: A Hellenistic capital in Anatolia* (pp. 354–375). Istanbul: Yapı Kredi Yayınları.

Kitov, G. (2003). *The valley of Thracian rulers*. Varna: Slavena.

Köhn, D., De Nil, D., Kurzmann, A., Przebindowska, A., & Bohlen, T. (2012). On the influence of model parametrization in elastic full waveform tomography. *Geophysical Journal International*, *345*, 325.

Köhn, D., Wilken, D., De Nil, D., Wunderlich, T., Rabbel, W., Werther, L., … Linzen, S. (2019). Comparison of time-domain SH waveform inversion strategies based on sequential low and bandpass filtered data for improved resolution in near-surface prospecting. *Journal of Applied Geophysics*, *160*, 69–83. https://doi.org/10.1016/j.jappgeo.2018.11.001

Krawczyk, C. M., Polom, U., Trabs, S., & Dahm, T. (2012). Sinkholes in the city of Hamburg—New urban shear-wave reflection seismic system enables high-resolution imaging of subrosion structures. *Journal of Applied Geophysics*, pp. 133–143.

Loke, M., & Barker, R. (1995). Least-squares deconvolution of apparent resistivity pseudosections. *Geophysics*, *60*(6), 1682–1690. https://doi.org/10.1190/1.1443900

Loke, M., Chambers, J., Rucker, D., Kuras, O., & Wilkinson, P. (2013). Recent developments in the direct-current geoelectrical imaging method. *Journal of Applied Geophysics*, *95*, 135–156. https://doi.org/10.1016/j.jappgeo.2013.02.017

Lütjen, H., & Utecht, T. (1991). Geophysikalische Untersuchungen auf dem Nemrud Dag (1989). *Nemrud Dag, Neue Methoden zur Archäologie* (pp. 31–38). Bönen: Münster.

Mangoldt, H. v. (2012). Makedonische Grabarchitektur. In *Wasmuth*. Tübigen: Die Makedonischen Kammergräber und ihre Vorläufer.

Mecking, R., Rabbel, W., & Erkul, E. (2015). Geophysikalische Prospektion am Yığma Tepe, in F. Pirson, Pergamon–Bericht über die Arbeiten in der Kampagne 2014. Archäologischer Anzeiger 2015/2, pp. 127–133. Retrieved from https://zenon.dainst.org/Record/001465043

**Mecking, R., Rabbel, W., & Erkul, E. (2016). Geophysikalische Prospektion am Yığma Tepe, in F. Pirson, Pergamon-Bericht über die Arbeiten in der Kampagne 2015. Archäologischer Anzeiger 2016/2, pp. 164–169. Retrieved from https://zenon.dainst.org/Record/001504669

Mecking, R., Rabbel, W., & Erkul, E. (2018). Geophysikalische Prospektion am Yığma Tepe, in F. Pirson, Pergamon - Bericht über die Arbeiten in der Kampagne 2017. Archäologischer Anzeiger 2018/2, pp. 137–142. Retrieved from https://zenon.dainst.org/Record/001580219

Mecking, R., Meinecke, M., Erkul, E., Bolten, A., Driehaus, B., Pirson, F., & Rabbel, W. (2020). The Yığma Tepe of Pergamon: Stratigraphic construction of a monumental tumulus from seismic refraction measurements. *Archaeological Prospection*, *27*(2), 73–105. https://doi.org/10.1002/arp.1762

**Mecking, R., Köhn, D., Meinecke, M., & Rabbel, W. (2020) (submitted). Cavity detection by SH-wave full waveform inversion—A reflection-focused approach. submitted to Geophysics.

Meinecke, M. (2019a). Ausgrabungen am tumulus Yığma Tepe, in F. Pirson, Bericht über die Arbeiten in der Kampagne 2017. Archäologischer Anzeiger 2018/2, pp. 129-136.

Meinecke, M. (2019b). Überlegungen zur Konstruktionsweise und zum Bauablauf amYığma Tepe, in F. Pirson, Bericht über die Arbeiten in der Kampagne 2017. Archäologischer Anzeiger 2018/2, pp. 142-147. Retrieved from https://zenon.dainst.org/Record/001580219

Milkereit, B., Stümpel, H., & Rabbel, W. (1986). Shear-wave reflection profiling for near-surface lignite exploration. *Geophysical Prospecting*, *34*, 845–855. https://doi.org/10.1111/j.1365-2478.1986.tb00497.x

Papadopoulos, N., Yi, M.-J., Kim, J.-H., Tsourlos, P.-I., & Tsokas, G.-N. (2010). Geophysical investigation of tumuli by means of surface 3D electrical resistivity tomography. *Journal of Applied Geophysics*, *70*(3), 192–205. https://doi.org/10.1016/j.jappgeo.2009.12.001

Parzinger, H., Gass, A., & Fassbinder, J. (2016). The foot of Royal Kurgans. *Science First Hand, The Controlled Explosion*, *43*(N1), 74–89.

Persson, K., & Olofsson, B. (2004). Inside a mound: Applied geophysics in archaeological prospecting at the Kings' Mounds, Gamla Uppsala, Sweden. *Journal of Archaeological Science*, *31*(5), 551–562. https://doi.org/10.1016/j.jas.2003.10.003

Philippson, A. (1912). Geographisch-geologische Übersicht der Landschaft. In A. Conze (Ed.), *Altertümer von Pergamon* (Vol. Bd. 1) (pp. 43–59). Berlin: Reimer.

Pirson, F. (2011). Der tumulus auf dem Ilyastepe und die pergamenischen Grabhügel. *Istanbuler Mitteilungen*, *61*, 120.

Pirson, F. (2016). Ausgrabungen am tumulus Yığma Tepe, in Bericht über die Arbeiten in der Kampagne 2015. *Archäologischer Anzeiger*, *2*, 158–164.

Pirson, F. (2017). Die Siedlungsgeschichte Pergamons-Überblick und kritische revision. *Istanbuler Mitteilungen*, *67*, 43–127.

Pirson, F., & Ludwig, B. (n.d.). Tumuli and natural sanctuaries: Visual aspects of urban space- and landscape-interaction in Hellenistic Pergamon and its micro-region. In C. G. Williamson (Ed.), *Sacred Lands, Connecting Routes. Religious Topographies in the Graeco-Roman world*.

Polymenakos, L., & Tweeton, D. (2017). Non-invasive characterization of a burial tumulus with use of seismic P-wave velocity and attenuation tomography. *Journal of Archaeological Science, Pp.*, *13*, 36–48. https://doi.org/10.1016/j.jasrep.2017.03.025

Polymenakos, L., Papamarinopoulos, S., Liossis, A., & Koukouli-Chryssanthaki, C. (2004). Investigation of a monumental Macedonian tumulus by three-dimensional seismic tomography. *Archaeological Prospection*, *11*, 145–158. https://doi.org/10.1002/arp.228

Rabbel, W. (2008). Seismic methods. In R. Kirsch (Ed.), *Groundwater geophysics* (pp. 23–83). Berlin, Heidelberg: Springer.

Radt. (2016). *Pergamon: Geschichte und Bauten einer antiken Metropole*. Darmstadt: Philipp von Zabern.

Roosevelt, C. (2003). *Lydian and Persian period settlement in Lydia*. Ithaca, New York: Cornell University.

Rose, C. B. (2014). *The archaeology of Greek and Roman Troy*. New York: Cambridge University Press.

Sandmeier, K.-J. (2019). REFLEXW version 8.5 windows™ XP/7/8/10-program for the processing of seismic, acoustic or electromagnetic reflection, refraction and transmission dat. Retrieved fromhttps://www.sandmeier-geo.de/download.html

Schön, J. H. (2015). *Physical properties of rocks: Fundamentals and principles of petrophysics*, *65*. Elsevier. https://www.elsevier.com/books/physical-properties-of-rocks/schon/978-0-08-100404-3

Shiyi, L., Guoyin, L., Bingqiang, Y., Qingbo, D., & Ping, H. (2006). Application of geophysical methods to explore the underground palace of the Emperor Qin Shi Huang Mausoleum. *SEG Technical Program Expanded Abstracts*, 481–485.

Stappmanns, V. (2012). Tumulus Taşdam Tepe, in F. Pirson, Bericht über die Arbeiten in der Kampagne 2011. Archäologischer Anzeiger 2012/2, pp. 241-248.

Stümpel, H., Kähler, S., Meissner, R., & Milkereit, B. (1984). The use of seismic shear waves and compressional waves for lithological problems of shallow sediments. *Geophysical Prospecting*, *32*, 662–675. https://doi.org/10.1111/j.1365-2478.1984.tb01712.x

Stümpel, H., Rabbel, W., & Schade, J. (1988). Oberflächennahe geophysikalische Untersuchungen im Mündungsgebiet des Río de Vélez und des Río Algarrobo. *Madrider Beiträge*, *14*, 60–72.

Tsokas, G., Tsourlos, P. I., Kim, J.-H., Yi, M.-J., Vargemezis, G., Lefantzis, M., … Peristeri, K. (2018). ERT imaging of the interior of the huge tumulus of Kastas in Amphipolis (northern Greece). *Archaeological Prospection*, 1–15.

Vafidis, A., Manakou, M., Kritikakis, G., Voganatsis, D., Sarris, A., & Kalpaxis, T. (2003). Mapping the ancient port at the archaeological site of Itanos (Greece) using shallow seismic methods. *Archaeological Prospection*, *10*(3), 163–173. https://doi.org/10.1002/arp.212

Vidale, J. E. (1988). Finite-difference calculation of travel times. *Bulletin of Seismological Society of America*, *78*((6)), 2062–2076.

Wölz, S., & Rabbel, W. (2005). Seismic prospecting in archaeology: A 3D shear-wave study of the ancient harbour of Miletus (Turkey). *Near Surface Geophysics*, *3*(4), 245–257. https://doi.org/10.3997/1873-0604.2005020

Wölz, S., Rabbel, W., & Müller, C. (2009). Shear waves in near surface 3D media - SH-wavefield separation, refraction time migration and tomography. *Journal of Applied Geophysics*, *68*(1), 104–116. https://doi.org/10.1016/j.jappgeo.2008.11.004

Yildirim, S. (2010). Askertepe tümülüsü. *Anatolia*, *36*, 149–178.

Yilmaz, Ö. (2001). *Seismic data analysis*. Tulsa: Society of Exploration Geophysicists. https://doi.org/10.1190/1.9781560801580

Ziegenaus, O. (1966). Hallenstraße, In: Boehringer, E. (Hrsg.), Die Ausgrabungen zu Pergamon im Jahre 1965. Vorläufiger Bericht mit Hinweisen auf Grabungen und Arbeiten früherer Jahre und des Frühjahres 1966. Archäologischer Anzeiger 1966, pp. 450–455. Retrieved from https://zenon.dainst.org/Record/000498177

**How to cite this article:** Mecking R, Meinecke M, Erkul E, Pirson F, Rabbel W. The Yığma Tepe of Pergamon: Internal construction of a monumental burial mound from shear wave reflection sounding and wavefield modelling. *Archaeological Prospection*. 2021;1–29. https://doi.org/10.1002/arp.1809

## APPENDIX A: REFLECTION SEISMIC

### A.1 | Details on the SH reflection seismic processing

Appendix A comprises additional information on the applied reflecthion semsic processing including tables of processing steps (Table A1) and acquisition parameters (Table A2) as well as some figures going into the specifics of the processing and obtained resolution:

- Resolution test via exploding reflector model (Figure A1)
- Information on the velocity model building (Figure A2)
- The effect of source-receiver offset restrictions in the CMP-Stack (Figure A3)
- Comparison of different poststack migration techniques (Figure A4)

**TABLE A1** General SH-wave reflection seismic processing

| |
|---|
| SH-wave reflection seismic processing |
| Geometry input |
| Quality check |
| Bandpass filter (10, 20, 80 and 100 Hz) |
| FK mute (if necessary) |
| Mute of noisy traces |
| Spherical divergence correction (RMS velocities) |
| Front mute of direct and surface waves (if necessary) |
| CMP binning along straight line |
| Datum correction to floating datum |
| NMO correction (RMS velocities) |
| Trace balance |
| CMP stack (offset <10 m) |
| Datum correction to fixed datum (below 73 m ASL) |
| FD migration (RMS velocities) |
| Semblance (dip-dependent)<br>Smoothing (max dip: 2 ms/trace) |
| Depth conversion (RMS velocities<br>Derived from Intervall velocity<br>Model SH0 (Figure 2) |

Abbreviations: CMP, common midpoint; FD, finite difference; NMO, normal moveout correction; RMS, root mean square.

**TABLE A2** Overview over the shown SH-seismic profiles

| Profile no. | Profile length (m) | Horizontal point source | Shot points | Shot point spacing (m) | Geophones (*) | Geophone spacing (m) |
|---|---|---|---|---|---|---|
| SH0 | 120 | Hammer + iron source 1 | 79 | 1–4 | 240 | 0.5 |
| SH12 | 120 | Hammer + iron source 1 | 50 | 2–4 | 240 | 0.5 |
| SH16 | 72 | Hammer + iron source 1 | 39 | 1–2 | 144 | 0.5 |
| SH20 | 72 | Hammer + iron source 2 | 45 | 1–2 | 144 | 0.5 |
| SH24 | 84 | Hammer + iron source 1 | 45 | 2–4 | 144 | 0.5 |
| OW20 | 84 | Hammer + iron source 2 | 44 | 2 | 168 | 0.5 |
| OW28 | 84 | Hammer + iron source 2 | 41 | 2 | 168 | 0.5 |
| OW36 | 84 | Hammer + iron source 2 | 38 | 2 | 168 | 0.5 |

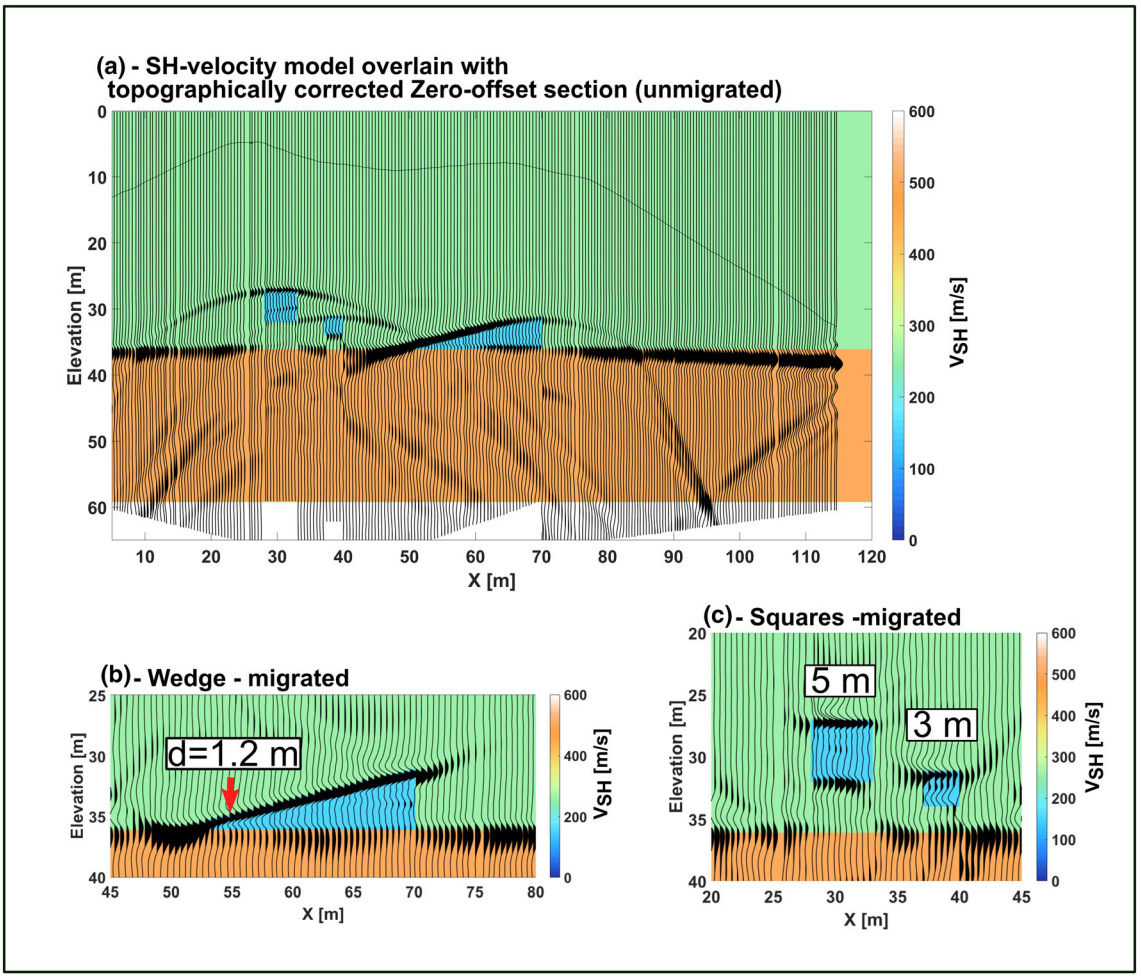


**FIGURE A1** Resolution study based on migrated zero-offset sections. (a) the topography of Profile SH0 is used. The Intervall velocity above the basal surface is set to 260 m/s corresponding to the root mean square (RMS) velocity at the basal surface on Profile SH0 and 500 m/s below the basal surface. The volumes with $V_{SH}$ = 100 m/s are inserted into the model. Two rectangles with 5- and 3-m side lengths respectively to demonstrate the lateral resolution and a wedge with a maximum height of 4 m to demonstrate the vertical resolution. Sources are set at each discontinuous gridpoint (0.1-m gridspacing). (b) The migrated section shows that at 1.2-m height a separation of top and bottom of the wedge is possible. (c) The 5-m column gets resolved well, whereas the 3-m volume shows some artefacts that lead to an overestimation of the size of the structure

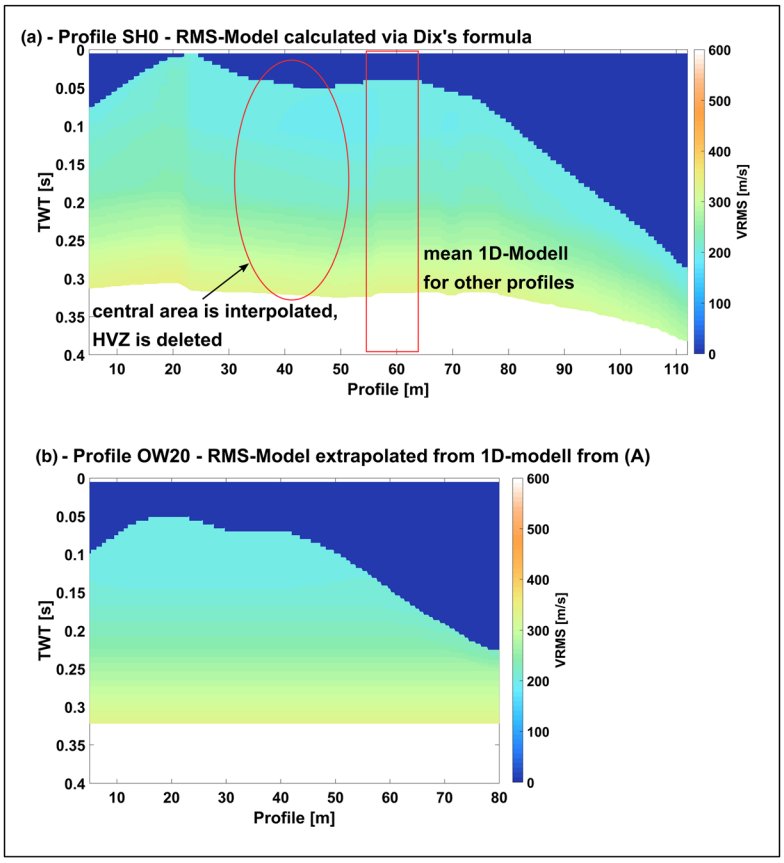


**FIGURE A2** Root mean square (RMS) velocity model derived from the interval velocity model of Profile SH0 (Figure 2b) via Dix's formula (Dix, 1955). The area around the high-velocity zone (HVZ) at the top of the mound (cf. Figure 2b) is ignored and the central area is interpolated. A mean 1D-model is calculated and extrapolated onto the other profiles where no refraction seismic analysis is possible (B). 0.25 s corresponds to the time where the reflection at the basal surface is expected

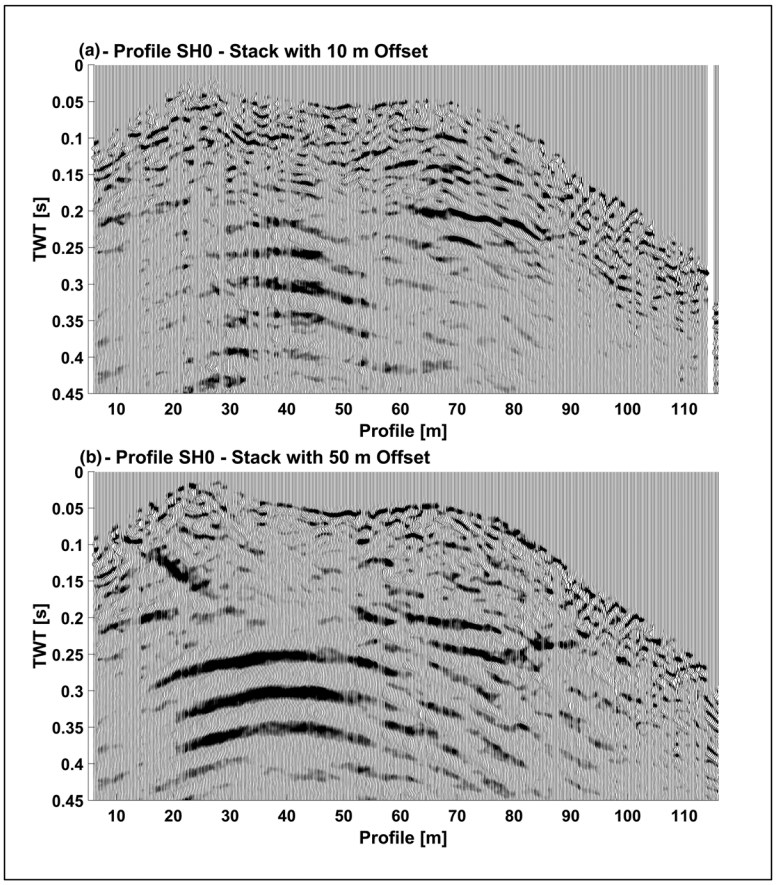


**FIGURE A3** Comparison of two stacks with different source–receiver offsets included in the common midpoint (CMP) gathers. (a) 10-m offsets shows higher resolution of near surface reflections compared to (b) 50-m offsets. Including higher offsets increases the resolution of deeper reflections but erases reflections in the upper 200 ms

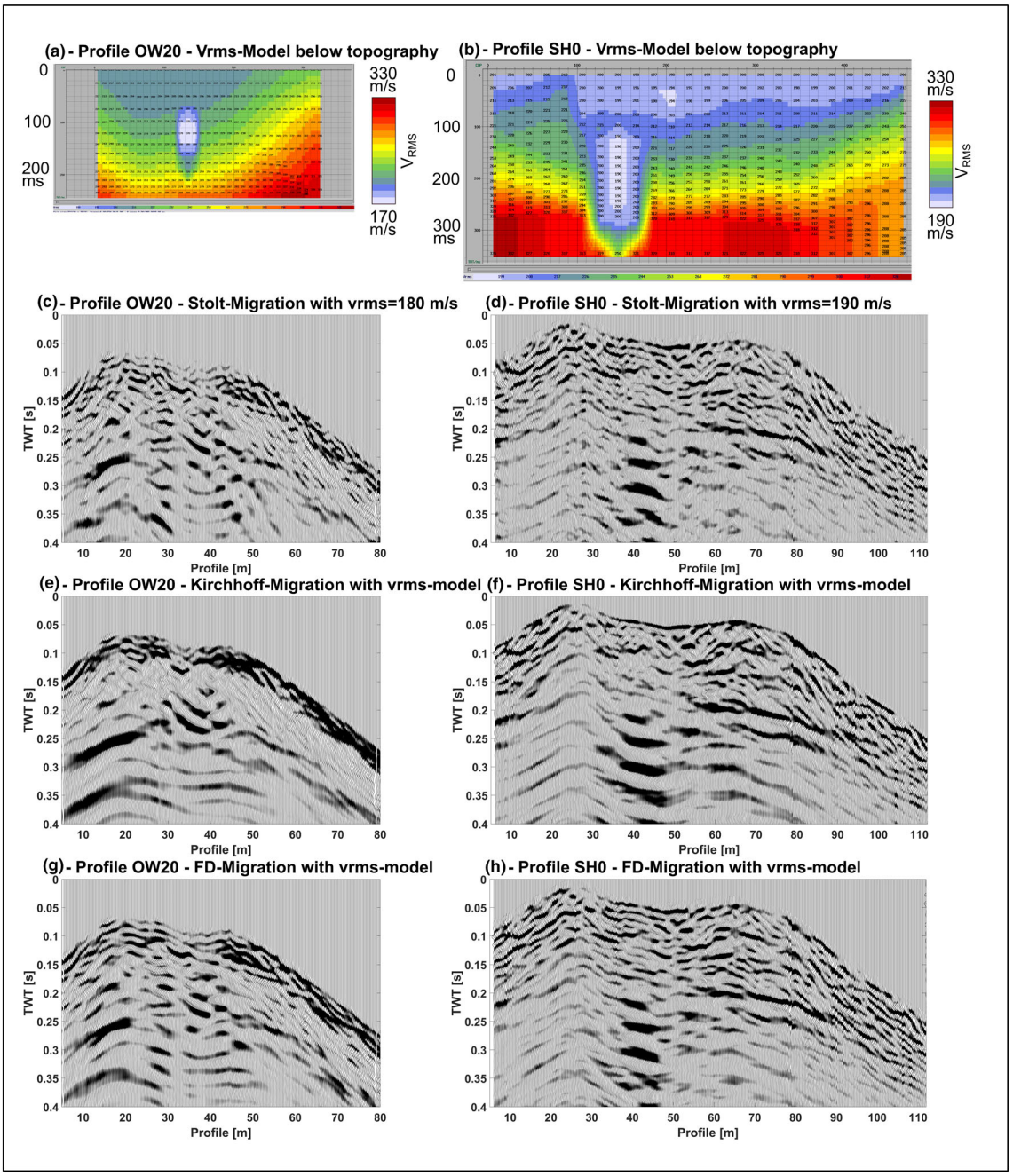


**FIGURE A4** Comparison of some of the post-stack migration techniques that have been tested on the reflection seismic sections shown on Profiles SH0 and OW20. (a, b) Velocity models with reduced topography and included volumes of reduced velocities around seismic object of interest (SOI) 1 and SOI 2. (c, d) Stolt migration shows reasonable good results, preserving the small-scale reflections but cannot incorporate lateral velocities thus leading to overmigration at SOI 2 (c). (e, f) Kirchhoff migration leads to strong smearing effects. (g, h) Finite difference (FD) migration shows good preservation of small-scale reflections while accurately migrating SOI 1 and SOI 2

## APPENDIX B: ELECTRICAL RESISTIVITY TOMOGRAPHY

### B.1 | Details on the geoelectric inversion

Appendix B shows the parameters used in the inversion of the ERT Profile EY263 (Table B1) as well as the modelled/measured data together with a graph showing the used block sizes (Figure B1). The trend of the RMS error for measured and calculated data points are given in Table 2. The inversion aborted in the seventh iteration as the convergence limit of <5% rel. change of RMS error was reached. The fourth iteration is used in the results as no structural changes appear in the fifth and sixth iteration but only some variation of the resitivities in the deeper parts of the model.

**TABLE B1** Computational parameters used for the electrical resistivity tomography of Profile EY263 with the RESINV2d software

| **Inversion parameters: Geoelectric Profile Y2 (finite element method with damped grid)** | |
|---|---|
| **Profile length** | **229 m** |
| Electrode spacing | 1 m |
| Configuration | Wenner-Alpha |
| Convergence limit rel. change of RMS error | 5% |
| Jacobi-matrix recalculation | Each inversion step |
| Increase of damping factor with depth | 1.05 |
| Robust data inversion constraint is used with cut-off factor | 0.001 |
| Robust model inversion constraint is used with cut-off factor | 0.001 |
| Effects of side blocks are severely reduced | |
| Thickness of the first layer | 0.5 m |
| Block width | See Figure B1 |

Abbreviation:RMS, root mean square.

**TABLE B2** RMS error values for Profile EY263

| Iteration | RMS error |
|---|---|
| 1 | 15.6 |
| 2 | 9.2 |
| 3 | 8.7 |
| 4 | 8.4 |
| 5 | 8.2 |
| 6 | 8.0 |

Abbreviations: RMS, root mean square.

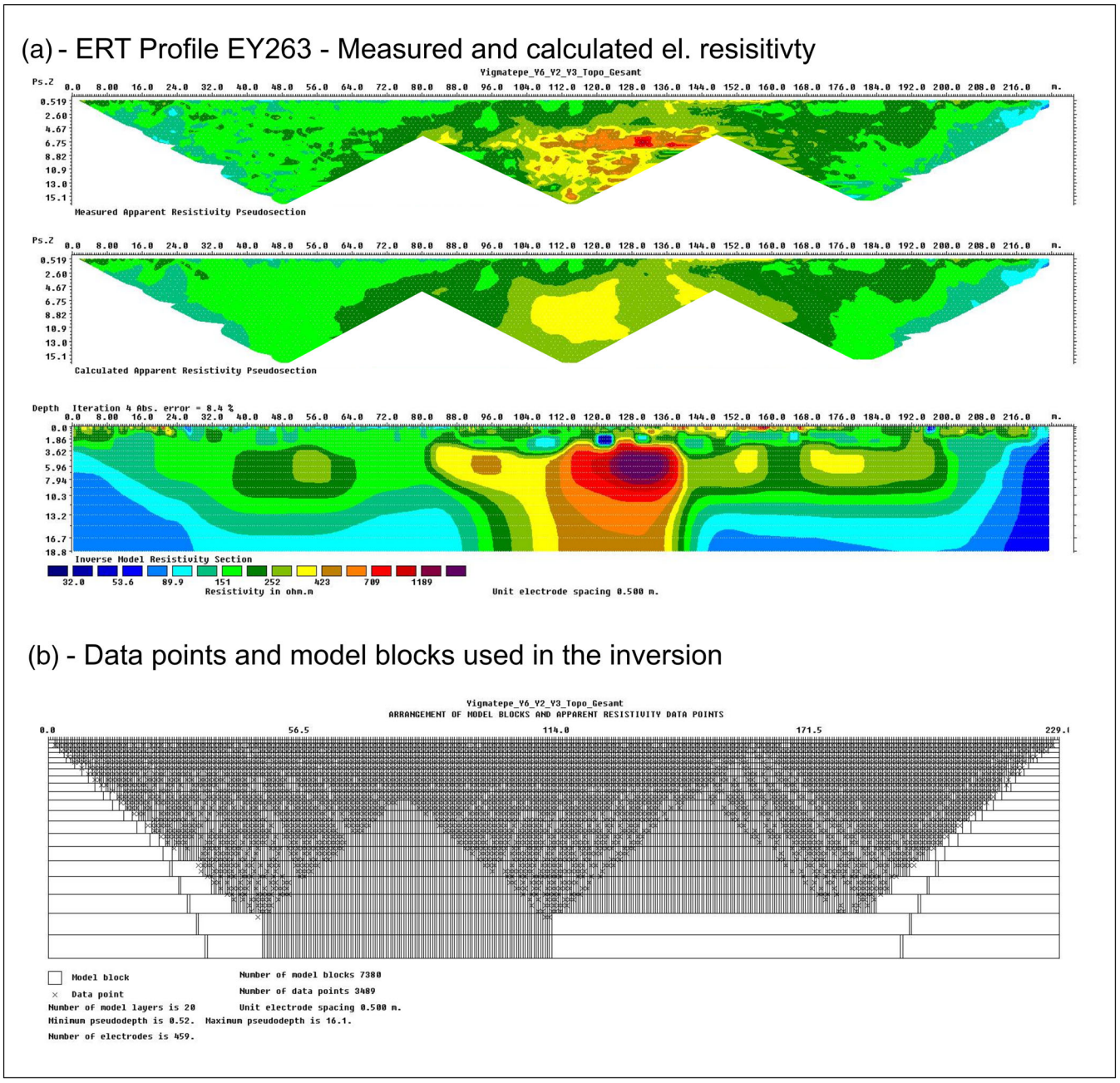


**FIGURE B1** Additional information concerning the inversion of electrical resistivity tomography (ERT) Profile EY263. (a) Measured and modelled apparent resistivity (top and centre, respectively) and the final inversion shown without the topography (bottom). (b) Locations of the model blocks and data points during the inversion

## APPENDIX C: SH-FORWARD MODELLING

### C.1 | Details on the SH-viscoelastic forward modelling

Appendix C comprises information on the parameters used in the forward modelling at Profiles SH0 and OW20 (Table C1). A visualization of the computed wavefield is given by snapshots in Figure C1, and some additional models for SOI 1 and SOI 2 are shown in Figures C2 and C3, respectively. They show how small changes in the model space lead to clearly visible changes in the modelled data.

**TABLE C1** FWM parameters

| Profile | Model width (m) | Model height (m) | Discretization (m) | Time sampling (s) | Max calc. time (s) | Source wavelet | Source frequency (Hz) | Damping factor Q |
|---|---|---|---|---|---|---|---|---|
| SH0 | 117 | 55 | 0.1 | 2e-5 | 0.5 | Spike | 10–80 | 40 |
| OW20 | 86.4 | 54.5 | 0.1 | 2e-5 | 0.5 | Spike | 10–80 | 40 |

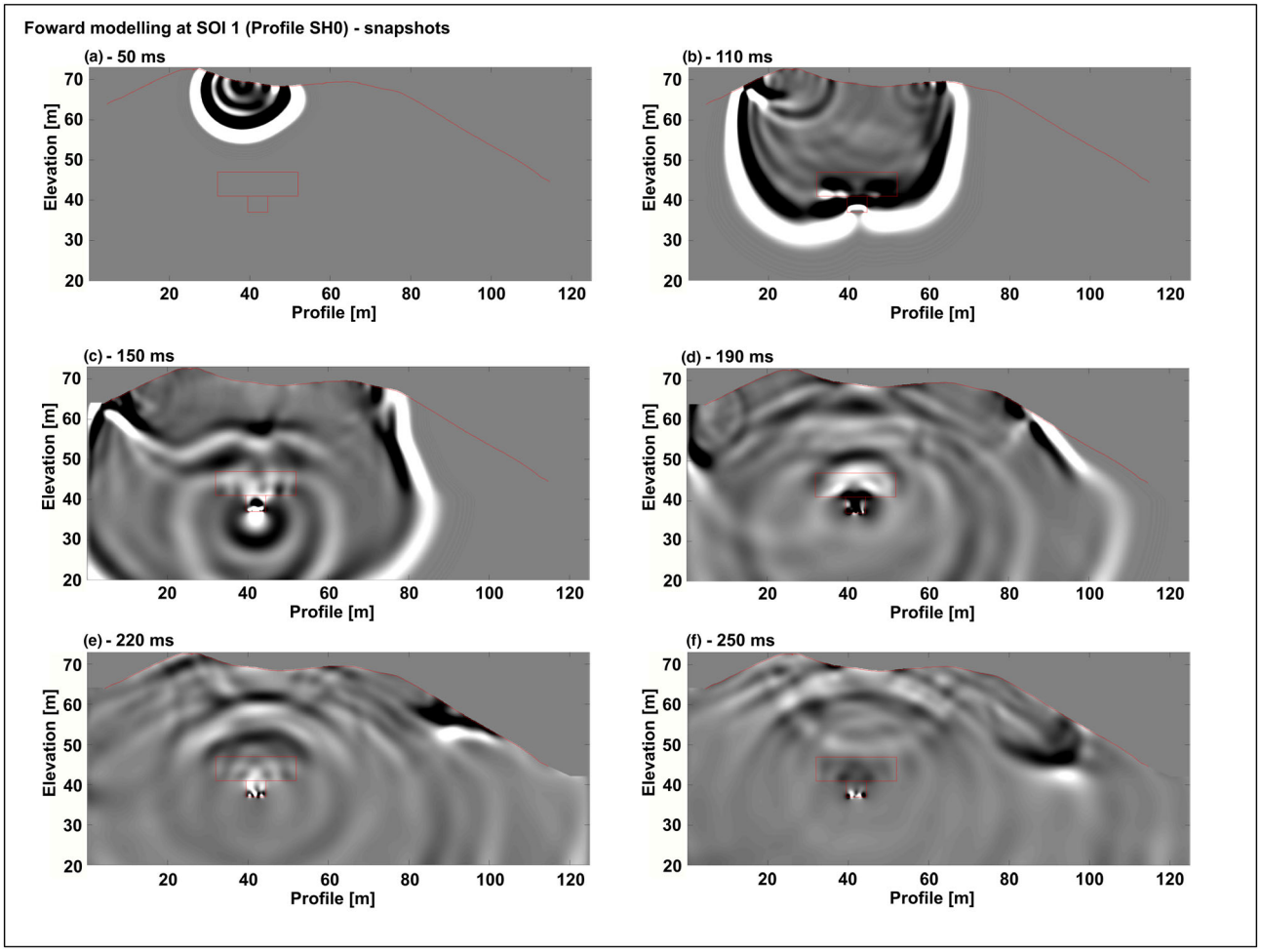


**FIGURE C1** (a) Snapshots of the forward modelled wavefield at the best fitting model for seismic object of interest (SOI) 1 (Figure 10e). (b) The wavefront gets reflected at the bottom of the low-velocity zone (LVZ). (d, e) Internal multiples are generated inside the smaller well generating 'pulses'

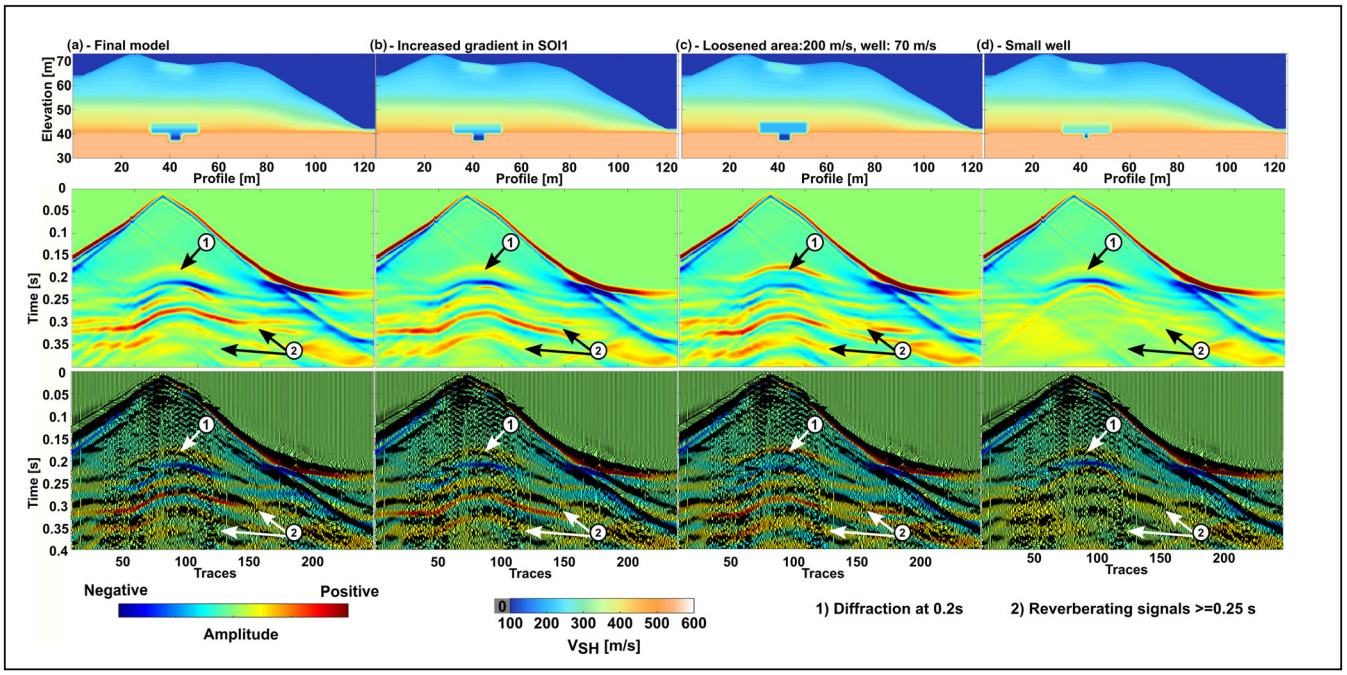


**FIGURE C2** Forward modelling tests at seismic object of interest (SOI) 1 in addition to Figure 10. (a) The final model for comparison. (b) The effect of increasing the negative velocity gradient with depth inside SOI 1. Later diffractions shift (Marker 2), increasing the gap between successive diffraction hyperbolae. (c) Setting the velocities inside SOI 1to a constant value of 220 and 70 m/s respectively. The reflection at the top of SOI 1 shows higher amplitude. (d) Decreasing the size of the well to 1.5 m. Most of the multiple diffractions vanish

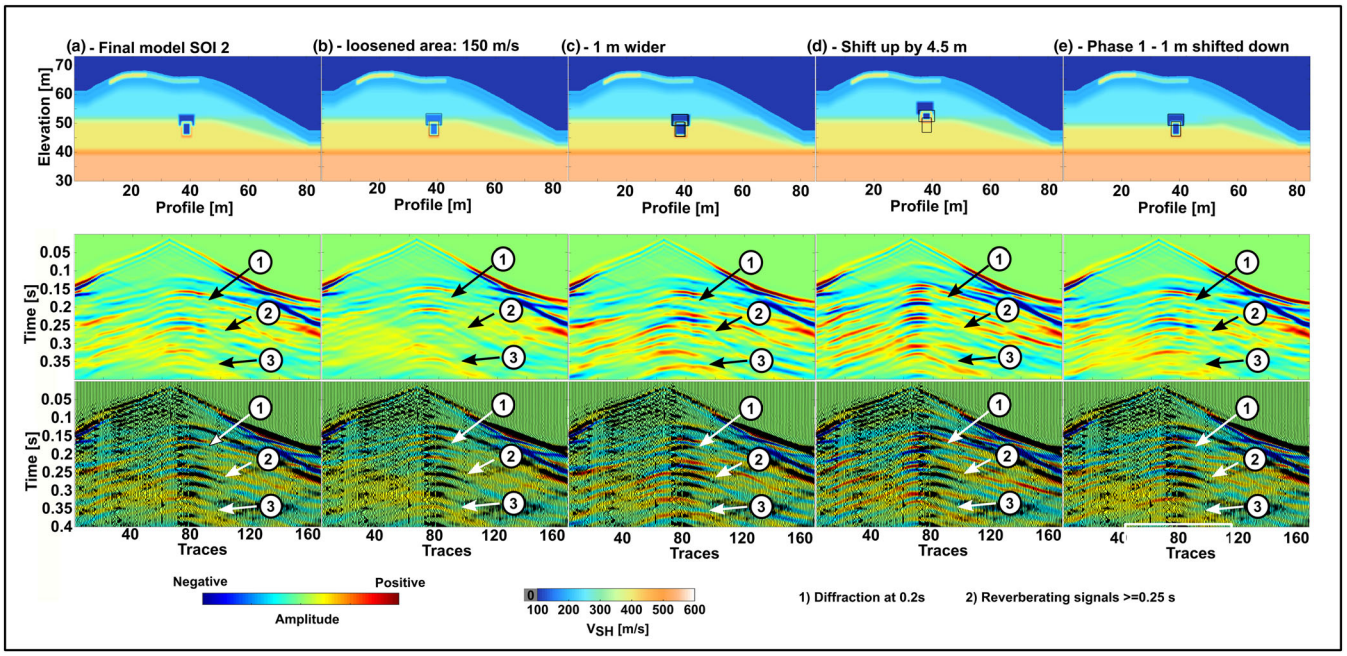


**FIGURE C3** Forward modelling tests at seismic object of interest (SOI) 2 in addition to Figure 11. (a) The final model for comparison. (b) Increasing the velocitiy inside both structures to 150 m/s instead of 110 m/s: The high-amplitude diffractions (Marker 2) vanish. (c) Increasing the width of the walled cavity by 1 m: the main diffraction gets separated into two overlapping diffractions whose apices are shifted in time. (d) Shifting SOI 2 upwards by 4.5 m leads to a similar pattern, but the apices appear shifted to the left. (e) Shifting SOI 2 downwards by 1 m into Phase 1 leads to flatter diffraction hyperbolae due to the increased velocities around the structure